ION CHANNELS

A pharmacological master key mechanism that unlocks the selectivity filter gate in K^+ channels

Marcus Schewe[1]*†, Han Sun[2]*, Ümit Mert[1], Alexandra Mackenzie[3,4,5], Ashley C. W. Pike[3], Friederike Schulz[1], Cristina Constantin[6,7], Kirsty S. Vowinkel[8], Linus J. Conrad[4,5], Aytug K. Kiper[8], Wendy Gonzalez[9,10], Marianne Musinszki[1], Marie Tegtmeier[1], David C. Pryde[11]‡, Hassane Belabed[12], Marc Nazare[12], Bert L. de Groot[13], Niels Decher[8], Bernd Fakler[6,7], Elisabeth P. Carpenter[3,4], Stephen J. Tucker[4,5], Thomas Baukrowitz[1]†

Potassium (K^+) channels have been evolutionarily tuned for activation by diverse biological stimuli, and pharmacological activation is thought to target these specific gating mechanisms. Here we report a class of negatively charged activators (NCAs) that bypass the specific mechanisms but act as master keys to open K^+ channels gated at their selectivity filter (SF), including many two-pore domain K^+ (K_{2P}) channels, voltage-gated hERG (human ether-à-go-go–related gene) channels and calcium (Ca^{2+})–activated big-conductance potassium (BK)–type channels. Functional analysis, x-ray crystallography, and molecular dynamics simulations revealed that the NCAs bind to similar sites below the SF, increase pore and SF K^+ occupancy, and open the filter gate. These results uncover an unrecognized polypharmacology among K^+ channel activators and highlight a filter gating machinery that is conserved across different families of K^+ channels with implications for rational drug design.

Dampening cellular electrical activity by pharmacological activation of specific types of K^+ channels has therapeutic potential for the treatment of a variety of disease states, including epilepsy, arrhythmias, vascular constriction, and various pain conditions (*1*, *2*). Consequently, screening efforts have identified a number of agents that open different types of K^+ channels (*2*), presumably by targeting their respective channel-specific activation mechanisms.

Distinct structural mechanisms enable K^+ channels to respond to a plethora of physiological stimuli, including voltage, temperature, mechanical force, and various second messengers, such as adenosine triphosphate (ATP), Ca^{2+}, and H^+, as well as bioactive lipids such as phosphatidylinositol 4,5-bisphosphate (PIP_2) and arachidonic acid (*3*, *4*). However, despite this complexity, these activation pathways seem to converge on the two principal mechanisms known to gate K^+ channels open: dilation of the "lower" gate at the intracellular pore entrance used by inwardly rectifying (K_{ir}) (*5*) and voltage-gated (K_v) K^+ channels (*6*), and activation of the selectivity filter (SF) gate used by most two-pore domain K^+ (K_{2P}) channels (*4*, *7*, *8*) and Ca^{2+}-activated big-conductance K^+ (BK_{Ca}) channels (*9*, *10*). In voltage-gated hERG (human ether-à-go-go–related gene) channels, both mechanisms coexist, with voltage opening the lower gate but rapid inactivation occurring through closure of the SF gate (*11*, *12*). Here we identify a common mechanism for drug-induced channel opening that bypasses these physiological activation mechanisms in SF-gated K^+ channels.

For the mechanosensitive K_{2P} channels TREK-1 and TREK-2, the voltage-gated hERG channel, and the Ca^{2+}-activated BK_{Ca} channel, a series of small-molecule activators all harboring a negatively charged group (tetrazole or carboxylate) have been proposed to act as selective channel openers [i.e., BL-1249 for TREK-1/-2 (*13*); PD-118057 for hERG (*14*); and NS11021 for BK_{Ca} (*15*)]. However, application of these compounds to their respective "nontarget" channels revealed an unexpected polypharmacology: All three openers displayed equal efficiency in opening TREK-1 channels (Fig. 1A) and hERG channels (Fig. 1B), as well as BK_{Ca} channels (Fig. 1C), whose activation curve is strongly shifted to more negative voltages (fig. S1C). This suggests that these activators may not target channel-specific activation mechanisms and may instead share a common mechanism. In all cases, the compound-mediated effect was effectively antagonized by large quaternary ammonium ions (QA_L^+) such as tetra-pentylammonium (TPenA) or tetra-hexyl-ammonium (THexA) that are known to block K^+ channels at a site immediately below the inner entrance to the SF (*16*) (Fig. 1, A and B, and fig. S1C). Likewise, all these activators reduced the QA_L^+-mediated inhibition in these different K^+ channels (Fig. 1C and figs. S1, A and B, and S7, A and B). Furthermore, extended screening with BL-1249 also revealed potent activation of several other K_{2P} channels (TREK-2, TRAAK, TALK-1, TALK-2, THIK-1, and THIK-2; fig. S1D). Together, these data suggest that these negatively charged activators (NCAs) (BL-1249, PD-118057, and NS11021) act on a gating mechanism that is shared among these different classes of K^+ channels and that their action involves a site that overlaps with the conserved QA_L^+-binding site located below the SF.

A distinctive feature of all NCA-responsive K^+ channels is their gating by the SF, a mechanism that is intimately coupled to ion permeation (*17*, *18*). In K_{2P} channels, this coupling leads to pronounced activation by Rb^+, which displays an ion occupancy distinct to K^+ at the four SF K^+ binding sites (S1 to S4) that stabilizes the activated state of the SF gate (*17*). Interestingly, Rb^+ not only activated all NCA-responsive K_{2P} channels but also led to robust activation of BK_{Ca} and hERG channels (Fig. 1D). By contrast, Rb^+ failed to exert any activatory effect on K^+ channels gated at the helix-bundle crossing (i.e., K_{ir} and most K_v channels), as was observed for $K_v1.1$, $K_v1.5$, $K_v3.1$, and $K_{ir}1.1$ (Fig. 1D); consistent with this, these channels were also not activated by BL-1249 (fig. S2, A to E). Furthermore, cyclic nucleotide–gated channels that are also gated at the SF were not activated by BL-1249, indicating that the NCA mechanism may be specific to SF-gated K^+ channels (fig. S2F).

To gain further mechanistic insight into channel opening by the NCAs, we next investigated their binding by x-ray crystallography, cysteine-scanning mutagenesis, and atomistic molecular dynamics (MD) simulations. First, anomalous diffraction data were collected from TREK-2 channels cocrystallized with a brominated derivative of BL-1249 ($BL\text{-}1249^{Br}$) (Fig. 2A; fig. S3, A to C; and supplementary materials and methods). Although no discrete electron density was visible for BL-1249 itself, in anomalous difference maps, two bromine peaks were clearly visible per TREK-2 dimer (fig. S3, A and B) and the main-chain protein backbone showed excellent agreement with a previously crystallized high-resolution structure of TREK-2 [Protein Data Bank (PDB) 4XDJ] (*19*). Both bromine anomalous difference peaks were located at the entrance of the side fenestrations branching off the central pore cavity below the SF. Comparison with a structure

[1]Institute of Physiology, Christian-Albrechts University of Kiel, 24118 Kiel, Germany. [2]Leibniz-Forschungsinstitut für Molekulare Pharmakologie (FMP), Department of Structural Biology, 13125 Berlin, Germany. [3]Structural Genomics Consortium, University of Oxford, Oxford OX3 7DQ, UK. [4]OXION Initiative in Ion Channels and Disease, University of Oxford, Oxford OX1 3PN, UK. [5]Clarendon Laboratory, Department of Physics, University of Oxford, Oxford OX1 3PU, UK. [6]Institute of Physiology II, Albert-Ludwigs University of Freiburg, 79104 Freiburg, Germany. [7]Centers for Biological Signaling Studies CIBSS and BIOSS, 79104 Freiburg, Germany. [8]Institute of Physiology and Pathophysiology, Vegetative Physiology, Philipps-University of Marburg, 35037 Marburg, Germany. [9]Centro de Bioinformatica y Simulacion Molecular, Universidad de Talca, 3465548 Talca, Chile. [10]Millennium Nucleus of Ion Channels-Associated Diseases (MiNICAD), Universidad de Talca, 3465548 Talca, Chile. [11]Pfizer Worldwide Medicinal Chemistry, Neuroscience and Pain Research Unit, Portway Building, Granta Park, Great Abington, Cambridgeshire CB21 6GS, UK. [12]Leibniz-Forschungsinstitut für Molekulare Pharmakologie (FMP), Department of Medicinal Chemistry, 13125 Berlin, Germany. [13]Computational Biomolecular Dynamics Group, Max Planck Institute for Biophysical Chemistry, 37077 Göttingen, Germany.
*These authors contributed equally to this work.
†Corresponding author. Email: m.schewe@physiologie.uni-kiel.de (M.S.); t.baukrowitz@physiologie.uni-kiel.de (T.B.) ‡Present address: Curadev Pharma Ltd., Sandwich Kent, UK.

that included QA_L^+ (*16*) showed that these bromine positions reside within the spherical volume of THexA but outside that of the smaller tetra-ethyl-ammonium (TEA) ion. Consistent with this, BL-1249 activation of TREK-2 channels was antagonized by THexA but not by TEA (Fig. 2, B and C).

These structural data were complemented by cysteine-scanning mutagenesis of the pore-lining M2 and M4 helices of TREK-1. Six residues, including the highly conserved Pro^{183} (P183) and Leu^{304} (L304) (also investigated in TREK-2, fig. S3D), were identified where mutations markedly reduced the apparent affinity of BL-1249. These residues cluster around the bromine densities

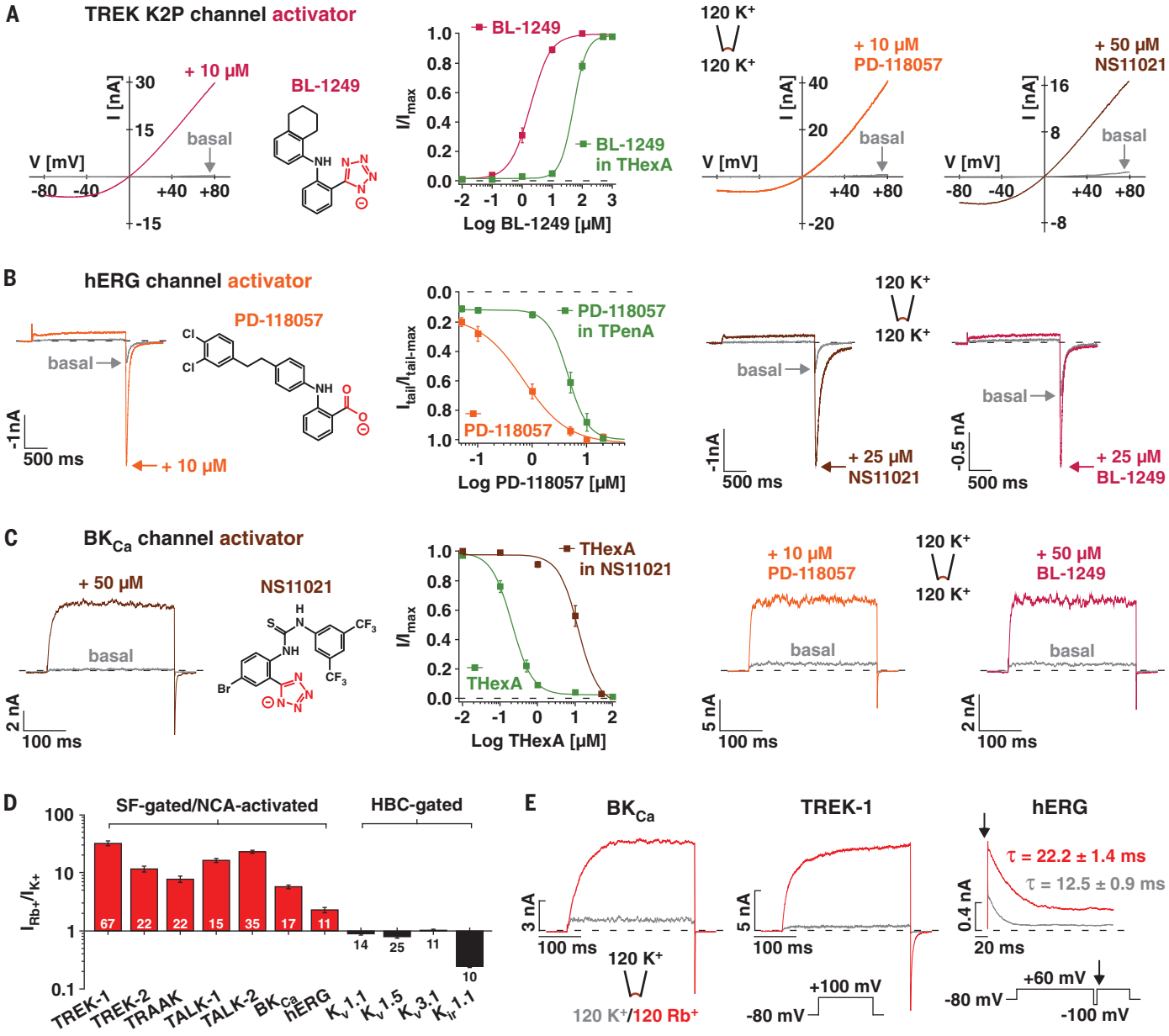

Fig. 1. NCAs open SF-gated K^+ channels via a similar site.
(**A**) Representative TREK-1 channel currents recorded in inside-out (i-o) patches evoked by voltage ramps in the absence (basal) and presence of the indicated compounds. BL-1249 (compound structure shown) dose-response curves represent currents at +40 mV and with or without 5 µM THexA that produced 77 ± 6% inhibition of basal currents ($n \geq 8$). I, current; V, voltage. (**B**) hERG channel currents (voltage steps from −80 to +60 mV) in i-o patches with or without the indicated compounds; arrows indicate peak tail current amplitudes at −100 mV. PD-118057 (compound structure shown) dose-response curves represent normalized tail currents with or without 1 µM TPenA that produced 91 ± 1% inhibition of basal currents ($n \geq 6$). (**C**) BK_{Ca} channel currents [voltage steps from a holding potential of −80 to +100 mV (zero Ca^{2+})] in i-o patches with or without the indicated compounds. THexA inhibition represents currents at +100 mV and with or without 50 µM NS11021 (compound structure shown; $n \geq 11$). (**D**) Rb^+ effects on different K^+ channels measured in i-o patches. Bars ± SEM represent fold change of outward currents upon exchange of intracellular K^+ by Rb^+ for K_{2P} and BK_{Ca} channels (+100 mV); for hERG, $K_v1.1$, $K_v1.5$, and $K_v3.1$ channels (+60 mV); and for $K_{ir}1.1$ channels (+40 mV). The channels are grouped as either SF-gated and NCA-activated or helix-bundle crossing (HBC)–gated. (**E**) Representative traces of Rb^+ activation for BK_{Ca}, TREK-1, and hERG channels using the indicated protocols [arrow indicates the starting point of hERG inactivation after inactivation recovery (at −100 mV)]. Time constant (τ) values from monoexponential fits to inactivation time course ($n \geq 12$). For (A) to (C), errors bars indicate SEM.

detected in the TREK-2 cocrystal with BL-1249^{Br} (Fig. 2D and fig. S3, C and D). A role for L304 in this presumed binding site was further supported by cysteine-modification protection experiments in which the time course of irreversible pore blockade induced by application of the cysteine-modifying agent MTS-TBAO [8-(tributylammonium)octyl methanethiosulfonate] (*20*) to TREK-1 L304C (Leu^{304}→Cys) channels was markedly slowed by the presence of BL-1249 (Fig. 2, E and F). This effect was specific for BL-1249, as two further channel activators with distinct binding sites [2-APB at the C terminus (*21*) and ML335 behind the SF (*22*)] both failed to slow this rate (Fig. 2, E and F). Furthermore, TREK-1 activation with 2-APB or ML335 was not antagonized by QA_L^+ inhibition, and mutations at the BL-1249 site did not affect 2-APB activation (fig. S4, A, B, and E).

In addition, we performed MD simulations to examine the orientation of BL-1249^{Br} within its proposed binding site (Fig. 2G). The favored binding pose oriented the negatively charged tetrazole group of BL-1249 toward the S6 "cavity binding site" for K^+ just below the SF. The remainder of the BL-1249 molecule engaged with residues in M2 and M4 consistent with our scanning mutagenesis data (Fig. 2D and fig. S3D). Moreover, the bromine atom in these simulations was found to be within 3 to 4 Å of the bromine densities determined by crystallography (fig. S3E). Together, these data indicate that BL-1249 binds to a site below the SF and reveal a critical role of the negative charge of the acidic tetrazole ring (pK_a around 5, where K_a is the dissociation constant), implying a pH-dependent compound efficacy. Indeed, when tested with the K_{2P} channel TALK-2 [exhibiting little intrinsic intracellular pH (pH_i) sensitivity], BL-1249 potency dropped strongly with a lowering of the solution pH_i to 5, whereas control experiments with 2-APB lacked this pH dependence (Fig. 3F).

We have recently used atomistic MD simulations and a double-bilayer setup to study ion permeation in the TRAAK K_{2P} channel (*17*). Therefore, we carried out simulations of ion permeation in

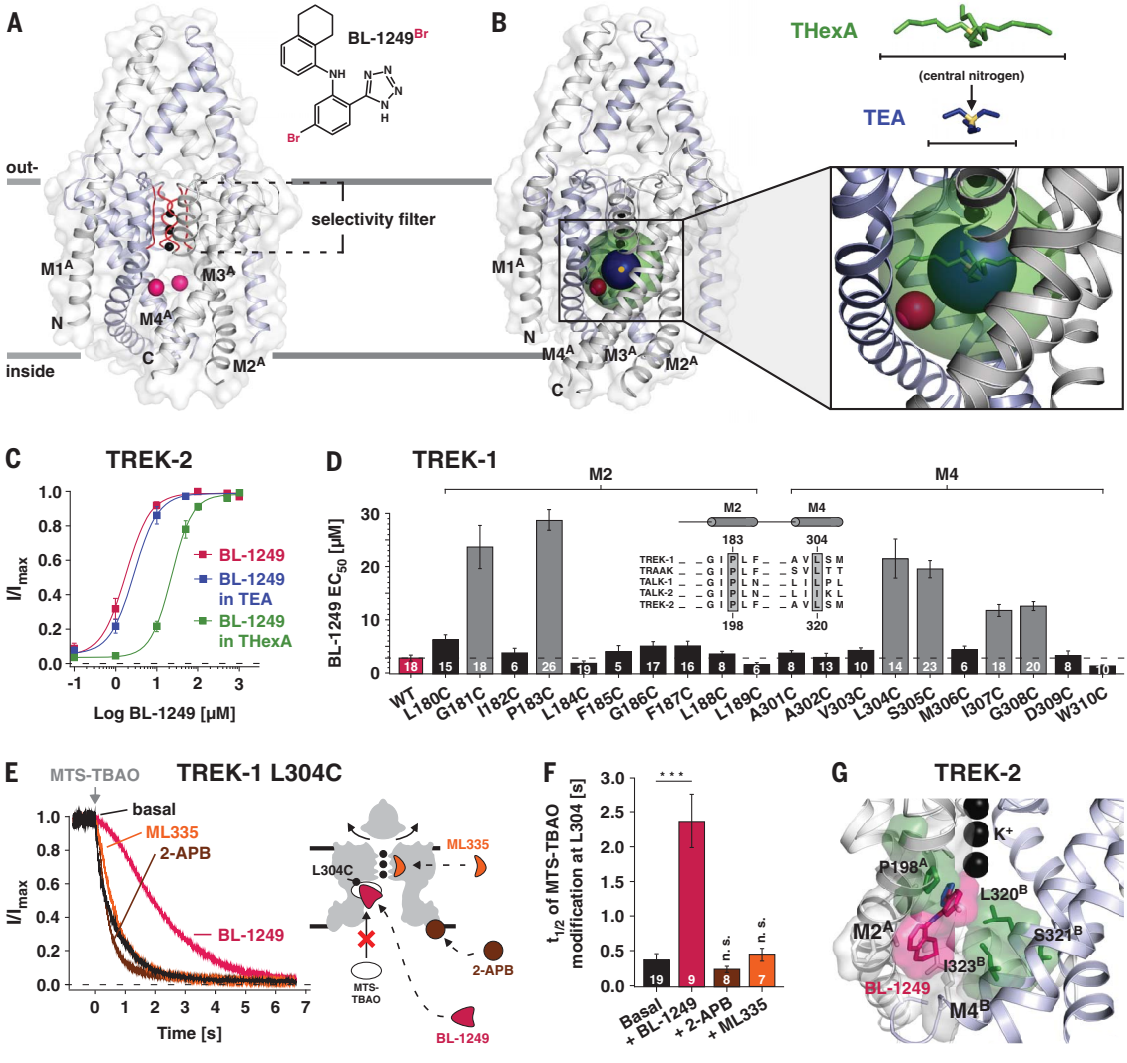

Fig. 2. Identification of the BL-1249 binding site in TREK K_{2P} channels. (**A**) The structure depicts TREK-2 (PDB 4XDJ), with pink spheres representing the positions of Br atoms in a brominated BL-1249 derivate (BL-1249Br) obtained by cocrystallization of TREK-2 and BL-1249Br (see also fig. S3). With this medium-resolution data, only the Br atoms were identified, because they gave peaks in anomalous difference maps. N, N terminus; C, C terminus. (**B**) The same structure also showing spherical representations of THexA (green) and TEA (dark blue) with their central nitrogen atoms (yellow). Their positions are based on the crystal structures of KcsA with QA^+s (*16*). Note that the Br atoms [pink spheres in (A)] are within the sphere of THexA but not of TEA. (**C**) BL-1249 dose-response curves for TREK-2 with or without 100 mM TEA ($n \geq 12$) or 5 μM THexA ($n \geq 13$) (TEA and THexA produce 74 ± 3 and 83 ± 2% basal current inhibition, respectively). Error bars indicate SEM. (**D**) Scanning mutagenesis of M2 and M4 helices showing BL-1249 median effective concentration (EC_{50}) values ± SEM determined at +40 mV; the inset shows a K_{2P} channel alignment for channels strongly activated by BL-1249 (see also fig. S1D) with residues homologous to TREK-1 P183 and L304 highlighted. (**E**) Time courses of 10 μM MTS-TBAO cysteine modification of L304C in TREK-1 before and after maximal activation by BL-1249 (50 μM), ML335 (50 μM), and 2-APB (1 mM) (left panel). The graphic depicts TREK-1 with predicted drug binding sites relative to the position of residue L304C. (**F**) Time values ± SEM for half-maximal MTS-TBAO modification inhibition ($t_{1/2}$) in the presence of different agonists. ***$P \leq 0.001$; n.s., not significant. (**G**) Representation of favored binding pose of BL-1249 (pink) in TREK-2 along with the location of the TREK-1 corresponding mutations (green) that reduce BL-1249 activation. For (A) and (G), the A and B superscripts indicate the subunit of the TREK-2 dimer. Single-letter abbreviations for amino acid residues are as follows: A, Ala; C, Cys; D, Asp; E, Glu; F, Phe; G, Gly; H, His; I, Ile; K, Lys; L, Leu; M, Met; N, Asn; P, Pro; Q, Gln; R, Arg; S, Ser; T, Thr; V, Val; W, Trp; and Y, Tyr.

TRAAK with BL-1249 modeled into the equivalent site in the TRAAK channel structure (PDB 4I9W) (Fig. 3A). This indicated several changes induced by BL-1249: (i) K^+ occupancy at the S6 site located adjacent to the negatively charged tetrazole group of BL-1249 increased ~16-fold (Fig. 3, A and B), (ii) K^+ occupancy of the S1 and S4 sites increased (Fig. 3B), and (iii) the rate of K^+ permeation increased by 1.6-fold (24 ± 2 ions/μs compared to 15 ± 2 ions/μs without BL-1249; Fig. 3C).

The effect of BL-1249 on ion permeation was further investigated with single-channel recordings of TREK-2 expressed in human embryonic kidney (HEK) 293 cells. Besides an increase in open probability, an increase in the measured single-channel amplitude was also observed in both the inward (from −29.3 ± 1.5 to −34.1 ± 1.9 pA at −100 mV; n = 7) and outward (from 17.7 ± 1.3 to 21.7 ± 1.4 pA at +100 mV; n = 7) directions in response to BL-1249 (Fig. 3, D and E). This result is consistent with the observed increase in SF ion occupancy at S1 and S4 that is expected to enhance ion permeation via a direct knock-on effect for ions entering the SF from either side (*23*). A similar increase in unitary conductance was also observed for TREK-1 channels recorded in patches from *Xenopus* oocytes (fig. S4, A to C). Notably, increases in single-channel conductance have not been observed upon activation of TREK-1, TREK-2, or TRAAK K_{2P} channels by other physiological stimuli (*24*, *25*).

Collectively, these results indicate that BL-1249 increases ion permeation and channel-open probability by influencing K^+ occupancy at sites below and within the SF. In line with this notion, mutations in the SF that change filter ion occupancy at the S1 and S4 sites (*17*, *26*) and induce the activated "leak mode" in K_{2P} channels (*17*) also render them insensitive to BL-1249 (and various other activators discussed below; fig. S6, A to D).

The negatively charged moiety identified within BL-1249, PD-118057, and NS11021 is also found in a series of known activators of TREK-1 and TREK-2 K_{2P} channels [ML67-33 (*27*), tetrazole; DCPIB (*28*), carboxylate], hERG channels [PD-307243 (*29*), carboxylate; NS3623 (*30*), tetrazole], and BK_{Ca} channels [GoSlo-SR-5-6 (*31*), sulphonate], and its requirement for channel activation has been demonstrated for ML67-33 and GoSlo-SR-5-6 (*27*, *31*). Indeed, these compounds also share all the hallmark features of BL-1249 action, including polypharmacology [i.e., mutual activation of K_{2P}, BK_{Ca}, and hERG channels (Fig. 4, C and D), sensitivity to QA_L^+ (Fig. 4A; fig. S7, A to C; and tables S2 and S3] and mutations that reduce BL-1249 activation in TREK-1 (fig. S4, C and D). In addition, MD simulations of their interaction with structures of the TREK-2, BK_{Ca}, and hERG channel pores identified similar stable binding poses below the SF with orientation of the negative moiety toward the cavity and a concomitant increase in K^+ occupancy at cavity and SF ion binding sites (Fig. 4, C and D, and figs. S7D and S8, A to C). Notably, this assumed NCA binding site overlaps with the "promiscuous inhibitor binding site" in the hERG channel, which underlies drug-induced long QT syndrome (*12*, *32*). This site is thought to accommodate many hydrophobic molecules (e.g., terfenadine), and consistent with this, we found that activation by PD-118057 strongly reduced inhibition by terfenadine (Fig. 4B).

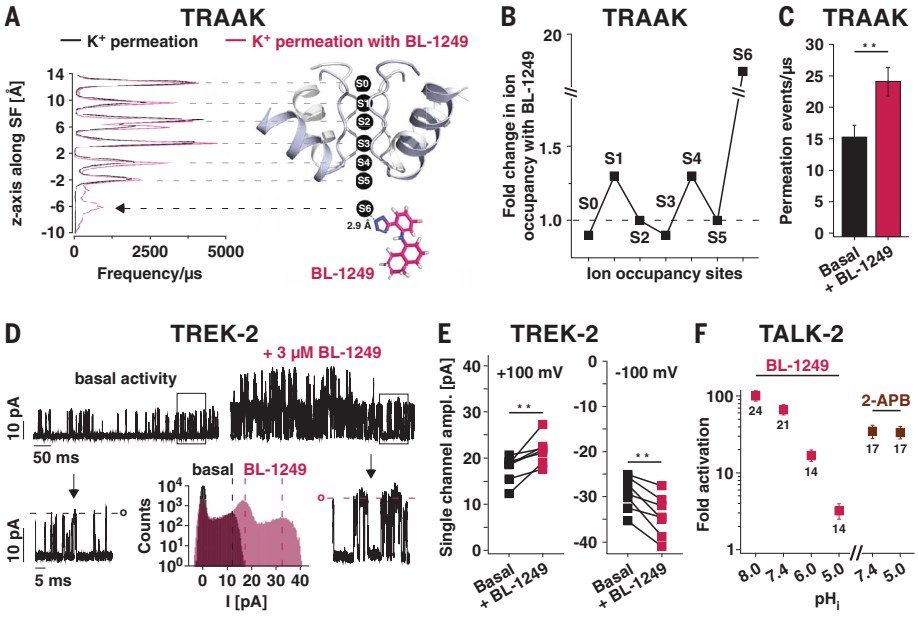

Fig. 3. Effects of BL-1249 on pore K^+ occupancy and permeation. (**A**) Ion occupancy (frequency/μs) of K^+ binding sites (S0 to S6) obtained from permeation MD simulations of TRAAK in the presence or absence of BL-1249, with BL-1249 adopting the identical position in TREK-2 (see Fig. 2G), that is, the negatively charged tetrazole ring (blue) in close proximity to the S6 K^+ ion. Coordinates were saved every 40 ps. The black arrow points to the increase in S6 K^+ occupancy. (**B**) Fold change in ion occupancy for the S0 to S6 sites. (**C**) MD simulations of K^+ permeation in TRAAK. Bars represent permeation events/μs from independent 200-ns MD simulations without (n = 50) and with BL-1249 (n = 30). $^{**}P \leq 0.01$. (**D**) Single-channel TREK-2 currents recorded at +80 mV from i-o patches before (basal) and after addition of 3 μM BL-1249, with arrows pointing to expanded scales of framed sections. The lower-middle panel depicts current amplitude histograms with or without 3 μM BL-1249 from i-o patches with ≤2 active channels (the right-hand peak represents the amplitude of two BL-1249–activated channels). Dotted lines indicate the single-channel amplitude maxima with or without BL-1249. (**E**) Paired single-channel current amplitudes before and after addition of 3 μM BL-1249 (n = 7). $^{**}P \leq 0.01$. (**F**) Fold activation of TALK-2 currents in i-o patches with 50 μM BL-1249 or 1 mM 2-APB applied at the indicated pH_i values. Error bars indicate SEM.

Our results uncover a class of K^+ channel openers, the NCAs, that act as a universal master key to unlock the SF gate. Mechanistically, these NCAs bind below the SF, where their negative charge promotes K^+ binding to the pore cavity, and thereby also alter the ion occupancy in the SF in a way that is known to promote activation of the filter gate (*17*). We hypothesize that, in particular, the increase at the S1 and S4 sites is responsible for activating the SF gate because all NCA-responsive channels are also activated by Rb^+ permeation, which is thought to increase ion occupancy at these sites, whereas mutations known to reduce S1 and S4 ion occupancy in K_{2P} channels abolish NCA activation. Furthermore, a loss of K^+ binding to the S1 site has been implicated in SF inactivation in K_v channels (*33*), hERG channels (*32*), and TREK-2 K_{2P} channels (*19*). However, at this time, we cannot exclude the possibility that nonelectrostatic interactions of the NCAs with their respective binding sites also contribute to the stabilization of the active SF state because these sites involve gating-sensitive regions [i.e., the TM4 (*8*, *19*) and S6 segments (*6*, *34*)]. In any case, our results support the view that many K_{2P} channels, as well as BK_{Ca} channels, adopt a low-activity (i.e., inactivated) state of their SF at rest and that the various physiological stimuli induce structural changes that drive the SF into an active (open) state. The NCAs appear to operate by means of bypassing these activation mechanisms to directly stabilize the SF in its active state.

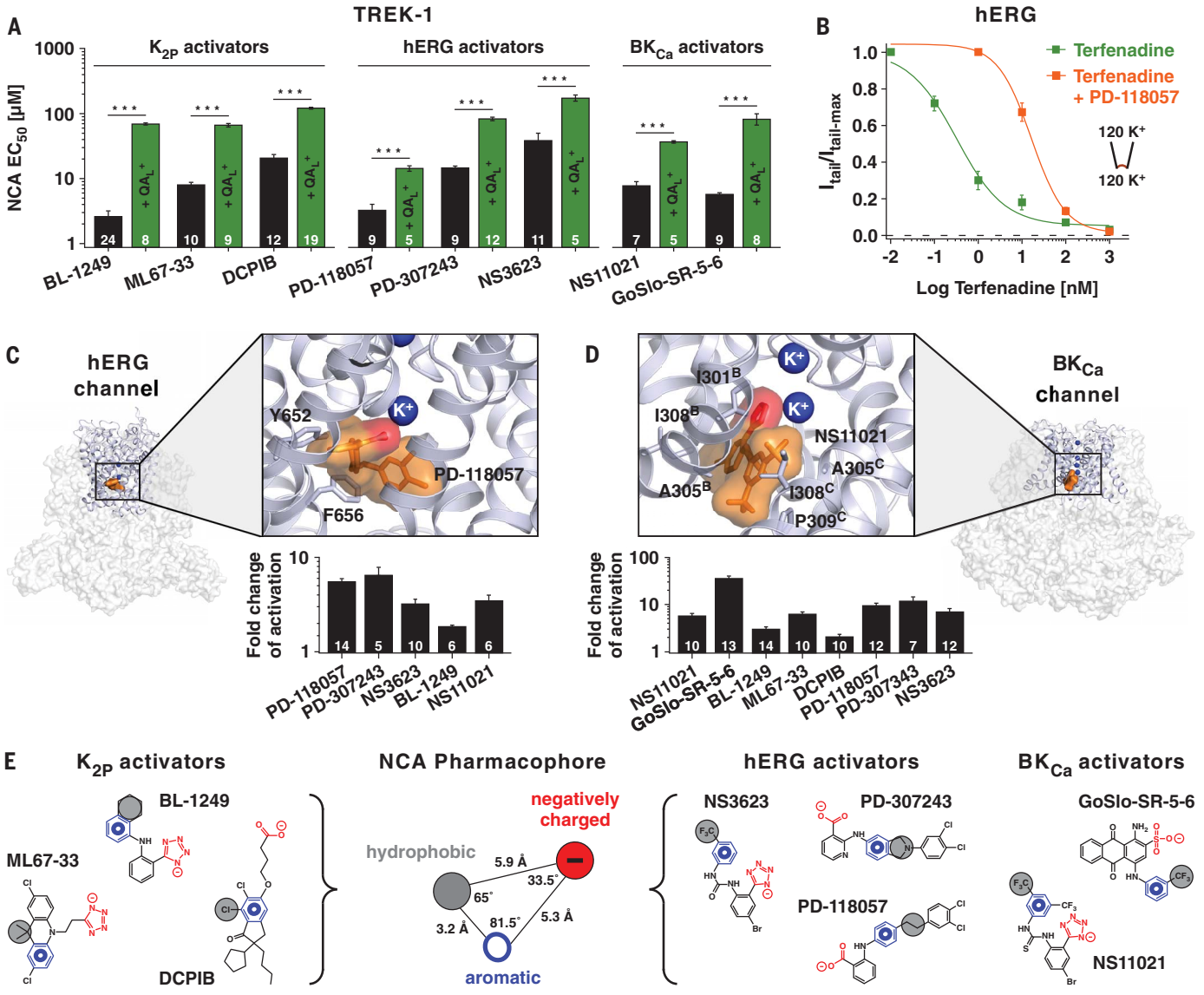

Fig. 4. NCA binding sites and common pharmacophores. (**A**) EC_{50} values (at +40 mV) for TREK-1 activation with compounds described as activators of either K_{2P}, hERG, or BK_{Ca} channels. Competitive antagonism is seen in the presence of QA_L^+ (either THexA or TPenA, which produce ~70 to 80% inhibition of respective basal K^+ currents). ***$P \leq 0.001$; error bars indicate SEM. (**B**) Terfenadine inhibition of hERG channels with or without 10 μM PD-118057. Error bars indicate SEM. (**C**) Structure of the hERG channel (PDB 5VA1) with the pore region expanded. This region was used for molecular docking and MD simulations to obtain the favored binding pose of PD-118057 (orange). Terfenadine-interacting residues are highlighted. The carboxylate group (red) interacts with a K^+ ion below the SF (see also fig. S7D); the bar chart below represents the fold activation of hERG tail currents at −100 mV with 10 μM of the indicated compounds. Error bars indicate SEM. (**D**) Same as in (C) but for the BK_{Ca} channel (PDB 5TJI), showing the favored binding pose of NS11021 (orange) where the tetrazole group (red) interacts with a K^+ ion below the SF and the residues in proximity to NS11021 highlighted. The bar chart below shows the fold activation of BK_{Ca} at +100 mV with 10 μM of the indicated compounds (at zero Ca^{2+}). Error bars indicate SEM; the B and C superscripts indicate the subunit of the tetramer. (**E**) Representation of the K_{2P}, hERG, and BK_{Ca} activators used to generate a common NCA pharmacophore consisting of aromatic (blue), hydrophobic (gray), and acidic (red) moieties, with distances and angles as shown.

In addition, our findings have important implications for the development of drugs that target K^+ channels, because they reveal the binding sites and the mechanism of action for many established activators in various K^+ channels. Our findings have also identified the first activators for several K_{2P} channels (e.g., TALK-1/-2 and THIK-1/-2). Notably, the NCA binding site overlaps with the promiscuous inhibitor site in hERG, and thus, targeting this NCA site might represent a promising approach to circumvent the drug-induced long QT syndrome, which is, as of now, a serious burden in drug development (*12*). However, the identified polypharmacology also represents a challenge for the development of any NCA-based compound into a highly subtype-specific K^+ channel agonist. Nevertheless, structural differences between K_{2P}, hERG, and BK_{Ca} channels may still permit a rational drug design that reduces this promiscuity. However, in some acute situations such as ischemic stroke or status epilepticus, exploiting the polypharmacology of NCAs to promote simultaneous opening of multiple neuroprotective K^+ channels (e.g., BK_{Ca}, TREK-1, TREK-2, TRAAK, THIK-1, and THIK-2) may even be beneficial.

REFERENCES AND NOTES

1. S. I. V. Judge, P. J. Smith, P. E. Stewart, C. T. Bever Jr., *Recent Pat. CNS Drug Discov.* **2**, 200–228 (2007).

2. V. K. Vyas, P. Parikh, J. Ramani, M. Ghate, *Curr. Med. Chem.* 10.2174/0929867325666180430152023 (2018).
3. S. Hou, S. H. Heinemann, T. Hoshi, *Physiology* **24**, 26–35 (2009).
4. M. I. Niemeyer, L. P. Cid, W. González, F. V. Sepúlveda, *Mol. Pharmacol.* **90**, 309–317 (2016).
5. F. V. Sepúlveda, L. Pablo Cid, J. Teulon, M. I. Niemeyer, *Physiol. Rev.* **95**, 179–217 (2015).
6. G. Yellen, *Nature* **419**, 35–42 (2002).
7. P. L. Piechotta *et al*., *EMBO J.* **30**, 3607–3619 (2011).
8. S. N. Bagriantsev, R. Peyronnet, K. A. Clark, E. Honoré, D. L. Minor Jr., *EMBO J.* **30**, 3594–3606 (2011).
9. C. M. Wilkens, R. W. Aldrich, *J. Gen. Physiol.* **128**, 347–364 (2006).
10. Y. Zhou, X.-M. Xia, C. J. Lingle, *Proc. Natl. Acad. Sci. U.S.A.* **108**, 12161–12166 (2011).
11. P. L. Smith, T. Baukrowitz, G. Yellen, *Nature* **379**, 833–836 (1996).
12. J. I. Vandenberg, E. Perozo, T. W. Allen, *Trends Pharmacol. Sci.* **38**, 899–907 (2017).
13. L. Pope *et al*., *ACS Chem. Neurosci.* **9**, 3153–3165 (2018).
14. J. Zhou *et al*., *Mol. Pharmacol.* **68**, 876–884 (2005).
15. B. H. Bentzen *et al*., *Mol. Pharmacol.* **72**, 1033–1044 (2007).
16. M. J. Lenaeus, D. Burdette, T. Wagner, P. J. Focia, A. Gross, *Biochemistry* **53**, 5365–5373 (2014).
17. M. Schewe *et al*., *Cell* **164**, 937–949 (2016).
18. J. G. McCoy, C. M. Nimigean, *Biochim. Biophys. Acta* **1818**, 272–285 (2012).
19. Y. Y. Dong *et al*., *Science* **347**, 1256–1259 (2015).
20. M. Rapedius *et al*., *Channels* **6**, 473–478 (2012).
21. R.-G. Zhuo *et al*., *Front. Cell. Neurosci.* **10**, 127 (2016).
22. M. Lolicato *et al*., *Nature* **547**, 364–368 (2017).
23. W. Kopec *et al*., *Nat. Chem.* **10**, 813–820 (2018).
24. M. V. Clausen, V. Jarerattanachat, E. P. Carpenter, M. S. P. Sansom, S. J. Tucker, *Proc. Natl. Acad. Sci. U.S.A.* **114**, E8343–E8351 (2017).
25. D. Kang, C. Choe, D. Kim, *J. Physiol.* **564**, 103–116 (2005).
26. M. Zhou, R. MacKinnon, *J. Mol. Biol.* **338**, 839–846 (2004).
27. S. N. Bagriantsev *et al*., *ACS Chem. Biol.* **8**, 1841–1851 (2013).
28. L. Minieri *et al*., *Br. J. Pharmacol.* **168**, 1240–1254 (2013).
29. E. Gordon *et al*., *Mol. Pharmacol.* **73**, 639–651 (2008).
30. R. S. Hansen *et al*., *Mol. Pharmacol.* **70**, 1319–1329 (2006).
31. S. Roy *et al*., *ChemMedChem* **7**, 1763–1769 (2012).
32. W. Wang, R. MacKinnon, *Cell* **169**, 422–430.e10 (2017).
33. V. Pau, Y. Zhou, Y. Ramu, Y. Xu, Z. Lu, *Nat. Struct. Mol. Biol.* **24**, 857–865 (2017).
34. H. Yang, G. Zhang, J. Cui, *Front. Physiol.* **6**, 29 (2015).

ACKNOWLEDGMENTS

We thank F. Lesage for the THIK-1 and THIK-2 K_{2P} channel clones; M. A. Hollywood for providing the BK_{Ca} activator GoSlo-SR-5-6; and J. Kusch for initially testing the BL-1249 effect on CNGA1 channels. We thank all members of our respective laboratories for technical support and comments on the manuscript. We thank Diamond Light Source Ltd. and its staff for access to the macromolecular crystallography beamlines. We also acknowledge the North-German Supercomputing Alliance (HLRN) for providing High Performance Computing (HPC) resources that have contributed to the research results reported in this paper. **Funding:** T.B. and B.L.d.G. were supported by the DFG; B.F. was supported by the DFG (SFB746, TRR 152, and EXC 294 and 2189); S.J.T. and E.P.C were supported by a BBSRC Industrial Partnership Award (BB/N009274/1); and L.J.C. was supported by a Wellcome Trust (OXION) Ph.D. studentship. A.M. was funded by the EPSRC Life Sciences Interface Doctoral Training Centre. A.C.W.P. and E.P.C. are members of the SGC (charity reference no. 1097737) funded by AbbVie, Bayer Pharma AG, Boehringer Ingelheim, the Canada Foundation for Innovation, Genome Canada, Janssen, Merck KGaA, MSD, Novartis, the Ontario Ministry of Economic Development and Innovation, Pfizer, São Paulo Research Foundation-FAPESP, and Takeda, as well as the Innovative Medicines Initiative Joint Undertaking ULTRA-DD grant 115766 and the Wellcome Trust 106169/Z/14/Z. D.C.P. was an employee of Pfizer at the time of the research. **Author contributions:** M.S. and T.B. conceived the study and designed the electrophysiological experiments. M.S., Ü.M., F.S., and M.T. performed all inside-out patch-clamp experiments in *Xenopus* oocytes. M.S. and T.B. analyzed the data. M.M. designed K^+ channel mutations. C.C. performed whole-cell recordings in CHO cells and analyzed the data together with B.F. Single-channel recordings in *Xenopus* oocytes were carried out and analyzed by K.S.V. and A.K.K., supervised by N.D. Single-channel recordings in HEK293 cells were performed and analyzed by L.J.C., supervised by S.J.T. A.M. purified TREK-2 and cocrystallized TREK-2 with BL-$1249^{Br.}$ A.M. and A.C.W.P. obtained and analyzed the x-ray data, supervised by E.P.C. and S.J.T. D.C.P. synthesized the brominated BL-1249. H.B. synthesized ML67-33, supervised by M.N. H.S. designed, performed, and analyzed all molecular dockings and MD simulations with critical comments of B.L.d.G. W.G. calculated and analyzed the NCA pharmacophore together with M.S. and N.D. M.S. and M.M. prepared and edited all figures. T.B., M.S., B.F., E.P.C., and S.J.T. contributed to the writing and editing of the manuscript and approved the manuscript. **Competing interests:** The authors declare no competing interests. **Data and materials availability:** All data are available in the main text or the supplementary materials. Requests for materials should be addressed to the corresponding authors.

SUPPLEMENTARY MATERIALS

9 August 2018; accepted 28 January 2019
10.1126/science.aav0569

A pharmacological master key mechanism that unlocks the selectivity filter gate in K^+ channels

Marcus Schewe, Han Sun, Ümit Mert, Alexandra Mackenzie, Ashley C. W. Pike, Friederike Schulz, Cristina Constantin, Kirsty S. Vowinkel, Linus J. Conrad, Aytug K. Kiper, Wendy Gonzalez, Marianne Musinszki, Marie Tegtmeier, David C. Pryde, Hassane Belabed, Marc Nazare, Bert L. de Groot, Niels Decher, Bernd Fakler, Elisabeth P. Carpenter, Stephen J. Tucker and Thomas Baukrowitz

Science **363** (6429), 875-880.
DOI: 10.1126/science.aav0569

A key to potassium channel activation

Using drugs to activate potassium channels has the potential to treat conditions like epilepsy, heart arrhythmias, and pain. Schewe *et al.* report a class of negatively charged activators (NCAs) with a defined pharmacore that use a similar mechanism to activate many types of potassium channels. X-ray crystallography, functional analysis, and molecular dynamics simulations showed that the NCAs bind below the selectivity filter to open the filter gate and activate the channels. Targeting this NCA site might be exploited in rational drug design.

Science, this issue p. 875

Supplementary Materials for

A pharmacological master key mechanism that unlocks the selectivity filter gate in K channels

Marcus Schewe*†, Han Sun*, Ümit Mert, Alexandra Mackenzie, Ashley C. W. Pike, Friederike Schulz, Cristina Constantin, Kirsty S. Vowinkel, Linus J. Conrad, Aytug K. Kiper, Wendy Gonzalez, Marianne Musinszki, Marie Tegtmeier, David C. Pryde, Hassane Belabed, Marc Nazare, Bert L. de Groot, Niels Decher, Bernd Fakler, Elisabeth P. Carpenter, Stephen J. Tucker, Thomas Baukrowitz†

*These authors contributed equally to this work.
†Corresponding author. Email: m.schewe@physiologie.uni-kiel.de (M.S.); t.baukrowitz@physiologie.uni-kiel.de (T.B.)

Published 22 February 2019, *Science* **363**, 875 (2019)
DOI: 10.1126/science.aav0569

This PDF file includes:

Materials and Methods

Molecular Biology and Experimental Electrophysiology

Rat K_{2P} TREK-1 (Genbank accession number: NM_172042), human K_{2P} TREK-2 (NM_021161), human K_{2P} TRAAK (NM_033310), human K_{2P} TALK-1 (NM_032115), human K_{2P} TALK-2 (EU978944), human K_{2P} THIK-1 (NM_022054), human K_{2P} THIK-2* Mbr based on (NM_022055; Mutations R11A, R12A, R14A, R15A, R16A and A155P), human ERG (EF00514521), human $K_v1.1$ (NM_004974), human $K_v1.5$ (NM_002234), human $K_v3.1$ (NM_001112741), rat $K_{ir}1.1$ (NM_017023), rat $K_{ir}2.1$ (NM_008425), mouse BK_{Ca} Δ0-65 (NM_001253378) and bovine CNGA1 (NM_174278.2) were used in this study.

Inside-out macropatch measurements. For K^+ channels expressed in *Xenopus laevis* oocytes the respective K^+ channel subtype coding sequences were subcloned into the pBF, pFAW or pSGEM vectors. Point mutations were introduced by site-directed mutagenesis using custom primers containing the desired mutation and finally verified by sequencing. Vector DNA was linearized with NheI or MluI and mRNA synthesized *in vitro* using the SP6 or T7 AmpliCap Max High Yield Message Maker Kit (Cellscript, Madison, USA) and stored in stock solutions at -80 °C. *Xenopus* oocytes were surgically removed from anesthetized adult females, treated with type II collagenase (Sigma-Aldrich) and manually defolliculated. About 50 nl of a solution containing the K^+ channel specific cRNA was injected into Dumont stage V - VI oocytes and subsequently incubated at 17 °C in a solution containing (mM): 54 NaCl, 30 KCl, 2.4 $NaHCO_3$, 0.82 $MgSO_4$ x 7 H_2O, 0.41 $CaCl_2$, 0.33 $Ca(NO_3)_2$ x 4 H_2O and 7.5 TRIS (pH 7.4 adjusted with NaOH/HCl) for 1 - 7 days before use. Electrophysiological recording: Macro patch recordings in inside-out configuration under voltage-clamp conditions were performed at room temperature (22 - 24 °C). Patch pipettes were made from thick-walled borosilicate glass, had resistances of 0.2 - 0.5 MΩ (tip diameter of 10 - 25 µm) and filled with a pipette solution (in mM): 120 KCl, 10 HEPES and 3.6 $CaCl_2$ (pH 7.4 adjusted with KOH/HCl). Intracellular bath solutions and compounds were applied to the cytoplasmic side of excised macro patches for the various K^+ channels via a gravity flow multi-barrel pipette system. Intracellular solution had the following composition (in mM): 120 KCl, 10 HEPES, 2 EGTA and 1 Pyrophosphate (pH adjusted with KOH/HCl). These patch pipette and intracellular solutions were used for recordings of K_{2P}, K_v and hERG channels (pH 8.0 for measuments of TREK-1/-2 WT and mutant channels to avoid pH activation; otherwise pH 7.4). For K_{ir} channels phosphatidylinositol-4,5-bisphosphate (PIP_2) was added to a final concentration of 10 µM to the intracellular bath solution to avoid

spontaneous run down. For CNGA1 channels the pipette and intracellular bath solution were (in mM): 150 KCl, 5 HEPES, 1 EGTA (pH 7.4 adjusted with KOH/HCl). For BK_{Ca} channels the pipette and intracellular bath solution were (in mM): 120 KNO_3, 10 HEPES, 10 EGTA (pH 7.4 adjusted with KOH/HNO_3). In other intracellular bath solutions, K^+ was replaced by Rb^+ either with Cl^- or NO_3^- as the counterion (pH 7.4 adjusted with RbOH/HCl or RbOH/HNO_3 respectively). Currents were recorded with an EPC10 amplifier (HEKA electronics, Germany) and sampled at 10 kHz or higher and filtered with 3 kHz (-3 dB) or higher as appropriate for sampling rate.

Chemical Compounds: Tetra-ethyl-ammonium chloride (TEA-Cl), tetra-pentyl-ammonium chloride (TPenA-Cl), tetra-hexyl-ammonium chloride (THexA-Cl), Guanosine-3`:5`-cyclic monophosphate (cGMP), (5,6,7,8-Tetrahydro-naphthalen-1-yl)-[2-(1H-tetrazol-5-yl)-phenyl]-amine (BL-1249), 2-aminoethoxydiphenyl borate (2-APB), losartan potassium, olmesartan, valsartan (Sigma-Aldrich), 2-[[4-[2-(3,4-Dichlorophenyl)ethyl]phenyl]amino]benzoic acid (PD-118057), *N*-[4-Bromo-2-(1*H*-tetrazol-5-yl-phenyl]-N'-[3-(trifluoromethyl)phenyl]-urea (NS3623), *N*'-[3,5-Bis(trifluoromethyl)phenyl]-*N*-[4-bromo-2-(2*H*-tetrazol-5-yl-phenyl]thiourea (NS11021), 4-[(2-Butyl-6,7-dichloro-2-cyclopentyl-2,3-dihydro-1-oxo-1*H*-inden-5-yl)oxy]butanoic acid (DCPIB) and α-[4-(1,1-Dimethylethyl)phenyl]-4-(hydroxydiphenylmethyl)-1-piperidinebutanol (terfenadine) (Tocris Bioscience), 8-(tributylammonium)octyl methanethiosulfonate bromide (MTS-TBAO-Br) (Toronto Research Chemicals, Inc.), phosphatidylinositol-4,5-bisphosphate (PIP_2) (Santa Cruz Biotechnology, Inc.), 2-[2-(3,4-Dichloro-phenyl)-2,3-dihydro-1H-isoindol-5-ylamino]-nicotinic acid (PD-307243), (*N*-[(2,4-dichlorophenyl)methyl]-4-(methanesulfonamido) benzamide) (ML335) (ChemBridge Corp.), (sodium 1-amino-4-((3-trifluoromethylphenyl)amino)-9,10-dioxo-9,10-dihydroanthracene-2-sulfonate) (GoSlo-SR-5-6) (provided by Mark Hollywood) and 2,7-Dichloro-9,9-dimethyl-10-[2-(1H-1,2,3,4-tetrazol-5-yl)ethyl]-4a,9a-dihydroacridine (ML67-33) (synthesized according to procedure previously described (*27*)) were stored as stocks (10 - 100 mM) at -80 °C and diluted in intracellular solution prior to the measurements or were added directly to a final concentration in intracellular solutions.

Data acquisition: Data analysis and statistics were done with Microsoft Excel 2011 (Microsoft Corporation, USA) and Igor Pro 6.34 software (Wavemetrics Inc., USA). The relative steady-state level of K^+ channel activation for the different activators was fitted with the Hill equation in the following form: $base + (max - base)/(1 + (x_{half}/x)^h)$, where base = basal current, max = maximal activated current, x = compound concentration, xhalf = value of

concentration for half-maximal occupancy of the compound binding site and h = Hill coefficient. Graphing was performed with Canvas X (ACD Systems of America, Inc., USA).

Single channel recordings. For single channel recordings of TREK-2 K_{2P} channels, HEK293 cells were transfected with human TREK-2 in pFAW (50 - 100 ng) using Fugene (Promega) and studied 18 - 24 h post transfection. The human TREK-2 sequence is the M3 variant, engineered to remove the multiple products of alternative translation initiation (*35*). Pipette resistance was 6 - 10 MΩ. Pipette and intracellular bath solution contained (in mM): 120 KCl, 10 HEPES and 2 EGTA (pH 7.2 adjusted with KOH/HCl). Excised patch recordings were made with an Axopatch 200B amplifier and Digidata 1550B A/D-Converter (Axon Instruments) with a 10 kHz bandwidth and a sampling rate of 50 kHz at room temperature (21 - 24 °C). 3 µM BL-1249 was applied via the intracellular bath solution. Data were analyzed using the single channel analysis tools: WinEDR (http://spider.science.strath.ac.uk/sipbs/software_ses.htm). For single channel recordings of TREK-1 K_{2P} channels expressed in *Xenopus laevis* oocytes pipettes had a tip resistance of 5.0 - 10.0 MΩ when filled with the pipette solution containing (in mM): 120 KCl, 10 HEPES, 3.6 $CaCl_2$ (pH 7.4 adjusted with KOH/HCl). Single channel currents were recorded with a sampling rate of 15 kHz with analog filter set to 5 kHz. Single channel amplitudes were evaluated from raw data histograms and kinetics were analyzed using the ClampFit10 software (Molecular Devices). For illustration the data were subsequently filtered with a -3 dB, 8-pole Bessel filter at 2 kHz using ClampFit10.

Whole-cell recordings. For whole-cell recordings of BK_{Ca} channels, Chinese hamster ovary (CHO) cells were transiently transfected with cDNA coding for the mouse BK_{Ca} channel alpha subunit and GFP. Cells were incubated at 37 °C and 5 % CO_2 and measured 2 - 4 days after transfection. Electrophysiological recording: Whole-cell patch-clamp recordings were performed at room temperature (21 - 24 °C) using a HEKA EPC10 amplifier. Currents were low-pass filtered at 3-10 kHz and sampled at 20 kHz. Leak currents were subtracted using a P/4 leak subtraction protocol with holding potential of -90 mV and voltage steps opposite in polarity to those in experimental protocol. Serial resistance was 30 - 70 % compensated using the internal compensation circuitry. The extracellular solution contained (in mM): 5.8 KCl, 144 NaCl, 0.9 $MgCl_2$, 1.3 $CaCl_2$, 0.7 NaH_2PO_4, 5.6 D-Glc and 10 HEPES (pH 7.4 adjusted with KOH/HCl). Recording pipettes pulled from quartz glass had resistance of 2-3.5 MΩ when filled with internal solution containing (in mM): 139.5 KCl, 3.5 $MgCl_2$, 2 DiBrBAPTA, 5 HEPES, 2.5 Na_2ATP and 0.1 Na_3GTP (pH 7.3). For some experiments THexA (50 µM) was added to the internal solution. Steady state activation of BK_{Ca} channels was determined using

test pulses ranging from -50 mV to +200 mV (with 10 mV increments), followed by a repolarization step to 0 mV. Conductance-voltage relations were determined from tail current amplitudes measured 0.5 ms after repolarization to a membrane potential of 0 mV and normalized to the maximum. For fitting, a Boltzmann equation was used in the form: $g/gmax = gmax/(1 + \exp((V_h - V_m)/k))$, where V_h is the voltage required for half-maximal activation and k the slope factor. All the chemicals except DiBrBAPTA (Alfa Aesar) were purchased from Sigma-Aldrich. Final concentration of the activator NS11021 was 30 µM.

Crystallography

Purification and co-crystallization of TREK-2 with brominated BL-1249. TREK-2 protein was purified as previously described (*19*). For co-crystallization, brominated BL-1249 ($BL\text{-}1249^{Br}$) dissolved in DMSO was added to purified TREK-2 giving a solution containing 10 mg/ml TREK-2, 5 mM $BL\text{-}1249^{Br}$, 5 % DMSO, 50 mM HEPES (pH 7.5), 200 mM KCl, 0.12 % OGNG, 0.012 % cholesteryl hemi-succinate (CHS), which was incubated on ice for 7 hours. Co-crystals of TREK-2 and $BL\text{-}1249^{Br}$ were obtained at 4 °C using sitting drops comprising 100 nl of protein/ligand solution and 50 nl of a reservoir solution containing 0.1 M Tris pH 7.5, 1 mM $CdCl_2$ and 29 % (v/v) polyethylene glycol (PEG)400, using a Mosquito crystallization robot (TTP Labtech). The brominated form of BL-1249 used in this study produces 94 ± 2 % (n = 6) of the peak whole-cell current of unmodified BL-1249 when applied at a concentration of 30 µM on TREK-2 channels expressed in *Xenopus* oocytes.

Anomalous diffraction data collection and location of bromine positions. Prior to mounting, crystals were incubated with an additional 7.5 mM $BL\text{-}1249^{Br}$ for 2 hours. The concentration of PEG400 was increased to 40 % in a step-wise manner prior to flash cooling. 920° of data were collected close to the Br K-edge (λ = 0.905 Å) on beamline I03 at the Diamond Light Source Ltd. Data were indexed and reduced using XDS (*36*) and scaled with XSCALE/AIMLESS (*37*). The final dataset has a nominal resolution of 4.1 Å (Mn I/sd I > 2.0) but displayed moderate anisotropy (3.8 Å x 4.1 Å x 4.9 Å - for details see table S1). Significant anomalous signal was detectable to around 6.5 Å ($CC_{anom} > 0.15$). The structure was solved by molecular replacement using PHASER (*38*) with the coordinates of the down-state TREK-2 structure as the initial model (PDB ID: 4XDJ). The crystals belong to space group $P2_1$ and the asymmetric unit contained two TREK-2 dimers. The positions of the bromine atoms and cadmium ions were located by calculating anomalous difference Fourier maps at 6 Å resolution. The two highest peaks (10.7 - 11.7 σ) in the map correspond to two cadmium ions that derived from the crystallization solution. The putative bromine atoms were

the next highest peaks in the map (4.1 - 6.2 σ). Two Br peaks could be located for each TREK-2 dimer with one site stronger than the other (AB dimer: 6.24/4.59 σ; CD dimer 4.11/4.97 σ). Regular crystallographic refinement with BUSTER (*39*) did not show any conventional electron density for either the bromine atoms or BL-1249 itself suggesting low occupancy and multiple binding modes. Given the lack of any conventional electron density, no attempt was made to model or refine a BL-1249^{Br}-TREK-2 complex structure based on the X-ray data. The positions of the bromine atoms shown in Fig. 2A and fig. S3 are based solely on real-space fitting to the peaks in the 6 Å anomalous difference map.

Molecular Dynamics Simulations

Molecular docking and MD simulations of the TREK-2 and TRAAK channels were based on their respective down-state crystal structures (PDB ID: 4XDJ (*19*) and PDB ID: 4I9W (*40*)). The hERG and BK_{Ca} (Slo1) structures were based on their respective cryo-EM structures (PDB ID: 5VA1 (*32*) and PDB ID: 5TJI (*41*)), where only the transmembrane domains M5 to M6 of hERG and BK_{Ca} channels were selected and simulated (residues 545 - 669 for hERG, residues 219 - 318 for BK_{Ca}). Missing loops in the cryo-EM structure of the hERG channel (residues 578 - 582, 598 - 602 in chains A to D) as well as missing side chains were built with the program MODELLER (*42*). We determined and evaluated the most probable binding poses for BL-1249, ML67-33, DCPIB, PD-307243, PD-118057, NS3623 and NS11021 with TREK-2, PD-118057 and PD-307243 with hERG as well as NS11021 and GoSlo-SR-5-6 with BK_{Ca} by a combination of X-ray crystallography, mutagenesis, molecular docking and molecular dynamics simulations. The procedures were performed as follows.

Binding pose of BL-1249 with TREK-2. Based on the results of a competition assay of BL-1249 with QA_L^+ blockers, we expected that BL-1249 binds within the pore cavity close to the known binding sites for QA_L^+ blockers in other K^+ channels. First, we used molecular docking to explore possible binding poses of BL-1249^{Br} with the down-state conformation of TREK-2, where the residues around the fenestration site were defined as the center of the docking pocket. A receptor grid was calculated for TREK-2 with a box size of 10 Å x 10 Å x 10 Å. Docking of the compounds into the pockets were subsequently carried out. 5 docking poses with highest scores were selected and further used as the initial structures in the first set of MD simulations. For each docking pose, 10 runs of 20 ns simulations were performed. We evaluated all possible binding poses sampled during the MD simulations and discarded those poses, which did not show interactions with residues L320 and P198 as suggested by mutagenesis studies, or significantly violated the coordinates of

bromine in BL-1249^{Br} bound to the TREK-2 channel as provided by the low-resolution X-ray data. At the end, two binding modes remained, both of which were stable in several 100 ns MD simulations. Although mutagenesis and low-resolution X-ray data did not allow us to distinguish between both binding modes, only one was chosen as the other was predicted to block the ion conduction pathway. Furthermore, only in this most binding mode were two BL-1249^{Br} molecules stable within one TREK-2 channel, which agreed well with the experimental data.

Binding poses of ML67-33, DCPIB and PD-307243 with TREK-2. Competition assays revealed that ML67-33, DCPIB, and PD-307243 bind in the same binding pocket of the TREK-2 channel as BL-1249. Therefore, as a first step a receptor grid was recalculated for TREK-2 and centered in the binding pose of BL-1249^{Br} with a box size of 10 Å x 10 Å x 10 Å. Docking of the compounds into the pockets was subsequently carried out and 5 poses for each ligand with highest docking scores were retained. The stability of each docking pose was evaluated and the binding poses were refined by 10 runs of 100 ns MD simulations. The most stable binding poses during the MD simulations were selected as the most probable binding modes.

Binding pose of PD-118057 with TREK-2. Due to remarkable structural similarities between PD-118057 and PD-307243, PD-118057 was manually aligned to the previously determined binding pose of PD-307243 in TREK-2. The pose of PD-118057 was further refined by 5 runs of 100 ns MD simulations. The most stable binding pose during the MD simulations was selected as the most probable binding mode.

Binding poses of NS3623 and NS11021 with TREK-2. Due to remarkable structural similarities between both NS ligands and BL-1249, NS3623 and NS11021 were manually aligned to the previously determined binding pose of BL-1249 in TREK-2. The poses of NS3623 and NS11021 were further refined by 5 runs of 100 ns MD simulations, respectively. The most stable binding poses during the MD simulations were selected as the most probable binding modes.

Binding poses of PD-118057 with hERG. Previous mutagenesis studies revealed a high-affinity drug binding site in the hERG channel pore (*43-45*) involving several residues (T623, S624, V625, G648, Y652 and F656) located near the central pore cavity (*32*). Given that this site also accommodates terfenadine and PD-118057 competes with terfenadine for binding, as starting point for the molecular docking, a receptor grid was calculated for the hERG channel with a box size of 10 Å x 10 Å x 10 Å, where these identified residues were defined as the centre of the docking pocket. Docking of the compounds into the pocket was subsequently

carried out. 5 docking poses with highest scores were selected and further used as the initial structures in MD simulations. The stability of each docking pose was evaluated, and the binding poses were refined by 10 runs of 100 ns MD simulations. The most stable binding poses during the MD simulations were selected as the most probable binding modes.

Binding poses of GoSlo-SR-5-6 and NS11021 with BK_{Ca}. Competition assays revealed that activation of the BK_{Ca} channel by GoSlo-SR-5-6 and NS11021 is antagonized by THexA, suggesting that the particularly large pore cavity below the selectivity filter could potentially accommodate these small molecule activators. Therefore, for the molecular docking a receptor grid with a larger box size of 15 Å x 15 Å x 15 Å that covers the pore cavity was calculated for the BK_{Ca} channel, where we chose the first residue of the selectivity filter (T276) as the centre of the box. Docking of the compounds into the pockets was subsequently performed. Only one docking pose for GoSlo-SR-5-6 and NS11021, respectively, was obtained with the negatively charged groups pointing to the center of the cavity. The stability of the docking poses was evaluated, and the binding poses were further refined by 5 runs of 100 ns MD simulations.

Methods for molecular docking. Molecular docking simulations of BL-1249^{Br}, ML67-33, DCPIB, PD-307243, PD-118057, NS3623 and NS11021 with the TREK-2 channel, of PD-118057 and PD-307243 with the hERG channel as well as of NS11021 and GoSlo-SR-5-6 with the BK_{Ca} channel were carried out with Glide from the Schrödinger package (*46*). Docking of the compounds into the channel pockets was performed with Glide SP (standard precision) from Schrödinger.

Molecular dynamics (MD) simulations. For the MD simulations, all ion channels were embedded in a hydrated 1-palmitoyl-2-oleoyl-phosphatidylcholine (POPC) lipid bilayer at an ionic concentration of 0.6 M KCl. We used the AMBER99sb* force field (*47*) and the TIP3P water model (*48*) for the equilibration and production simulations of the proteins. Parameters for ions and lipids were derived from (*49, 50*). All ligands were optimized and their electrostatic potentials were calculated at the Hartree-Fock/6-31G* level using the program Gaussian09. The generalized amber force field (GAFF) (*51*) topologies of the ligands were generated with the Antechamber software (*52*) using partial charges from quantum mechanics calculations according to the restrained electrostatic potential (RESP) approach (*53*). Tetrazole and carboxylic acid have pKa values of about 4.5 - 4.9 (*54*), indicating that both groups are non-protonated and negatively charged at pH 7.0. The sulfonate group in GoSlo-SR-5-6 activators is strongly acidic and negatively charged at pH 7.0. Protonation states of all protein residues were chosen to correspond to a pH value of 7.0. MD simulations

were carried out with GROMACS 5.0 and 5.1 (*55, 56*). Short-range electrostatic interactions were calculated with a cutoff of 1.0 nm, whereas long-range electrostatic interactions were treated by the particle mesh Ewald method (*57, 58*). The cutoff for van-der-Waals interactions were set to 1.0 nm. The simulations were performed at 300 K with a velocity rescaling thermostat (*59*). The pressure was kept at 1 bar by means of a semi-isotropic Parrinello-Rahman barostat (*60, 61*). All bonds were constrained with the LINCS algorithm (*62*). For the computational electrophysiology study (*63*), the equilibrated system of BL-1249^{Br} bound TRAAK was duplicated along the z direction and transmembrane potential gradients were generated by introducing a charge difference of 2 K^+ ions between the two compartments separated by the two lipid bilayers. During the MD simulations, the number of the ions was kept constant by an additional algorithm (*63*). The resulting membrane potential can be calculated by double-integration of the charge distribution using the Poisson equation as implemented in the GROMACS tool *g_potential* (*64*). In the computational electrophysiology simulations of BL-bound TRAAK, a K0KK0K (S0, S1, S2, S3, S4, S5) ionic configuration was employed as the starting structure, as it was the largest populated ionic configuration in MD simulations of apo-TRAAK (*17*) and KcsA (*65*) using the same method. This ionic configuration is consistent with a direct knock-on mechanism of potassium conduction. Notably, our previous study revealed that the permeation mechanism does not depend on the exact starting configuration (*65*). In order to prevent spontaneous dissociation of ligand during the permeation simulation, we restrained the position of bromine of BL-1249^{Br} at the crystallographically determined position with a harmonic force constant of 1000 kJ mol^{-1} nm^{-2}. During the simulations a permeation event was counted when an ion moved from the cavity to the filter, and another ion left the S0 position. The computational electrophysiology simulations of apo-WT TRAAK were described in previous work (*17*).

Molecular Pharmacophore Modeling

The required interactions between a K_{2P} channel and a ligand depend on structural and chemical complementarity among them. We used PHASE from Schrödinger molecular modeling Suite (*66*) to generate a pharmacophore. PHASE categorizes the chemical characteristics of the ligands as hydrogen bond acceptors (A), hydrogen bond donors (D), hydrophobic groups (H), negatively charged groups (N), positively charged groups (P) and aromatic rings (R). In order to develop a common pharmacophore, PHASE evaluates the n-point pharmacophores resulting from the conformational sets of active compounds and then

detects all three-dimensional arrangements with pharmacophore qualities common for these compounds (*67*).

Statistical analyses

All values are represented as mean ± S.E.M. with n indicating the number of individual executed experiments. Error bars in all figures represent S.E.M. values with numbers at base (n) indicating the definite number of executed experiments. A Shapiro-Wilk test or Kolmogorow-Smirnow test was used to determine whether measurements were normally distributed. Statistical significance between two groups was validated using the Student`s *t*-test or Wilcoxon rank test after *f*-test application. Asterisks indicate the following significance: * ≤ 0.05, ** ≤ 0.01 and *** ≤ 0.001. Zero current level was indicated using dotted lines in all figures.

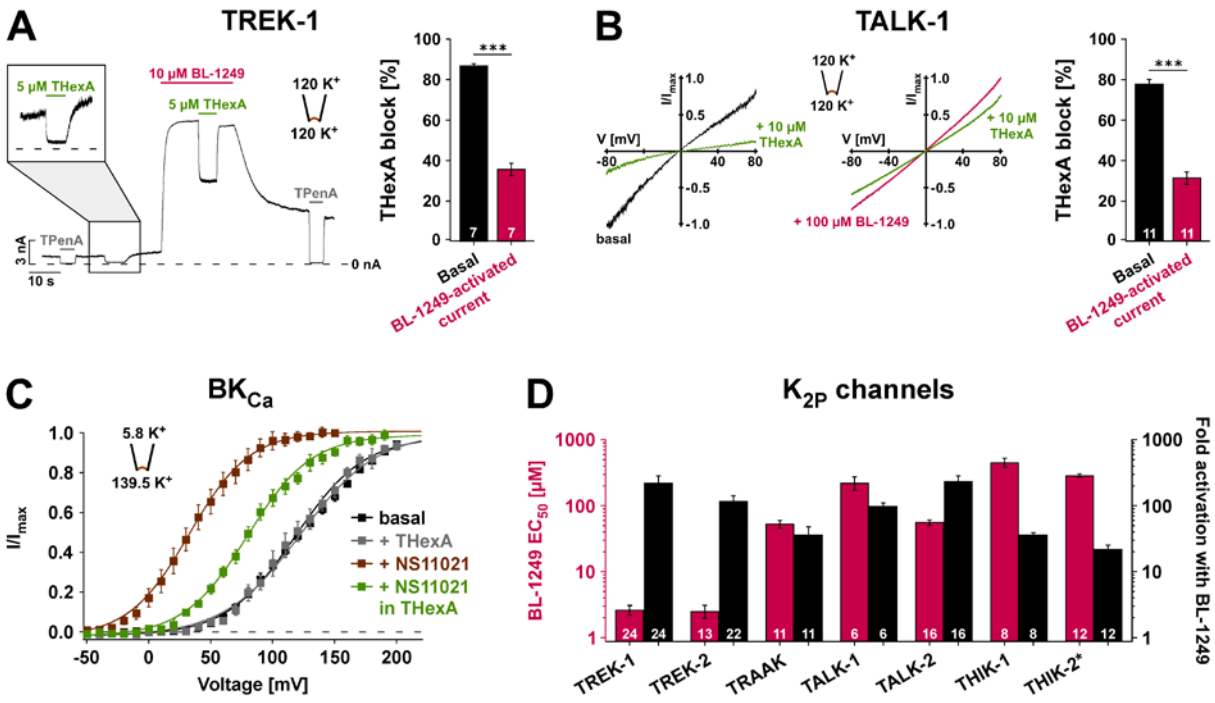

Fig. S1. Activation of K^+ channels (K_{2P} and BK_{Ca}) and competitive antagonism by QA_L^+.

Fig. S1. Activation of K^+ channels (K_{2P} and BK_{Ca}) and competitive antagonism by QA_L^+. (**A**) Left: TREK-1 currents at +40 mV upon application of 1 mM TPenA (full inhibition) and 5 µM THexA in the absence (basal current) and presence of 10 µM BL-1249; right: bars represent THexA inhibition ± BL-1249 from experiments as shown in the left panel. (**B**) Left: TALK-1 currents evoked by voltage ramps from -80 mV to +80 mV (black trace; basal) and inhibition by 10 µM THexA (green trace); middle: TALK-1 currents activated by 100 µM BL-1249 (pink) and subsequent inhibition by 10 µM THexA (green); right: bars represent THexA inhibition ± BL-1249 from experiments as shown in the left and middle panels. (**C**) Current-voltage relations from BK_{Ca} channel whole-cell tail current amplitudes (I/I_{max}) in presence of 30 µM NS11021, 50 µM THexA, 30 µM NS11021 with 50 µM THexA, and without compounds (basal); lines represent fits to a standard Boltzmann function ($n \geq 8$). (**D**) Bars represent EC_{50} values ± S.E.M. and maximal fold activation ± S.E.M. for the indicated K_{2P} channel upon application of BL-1249.

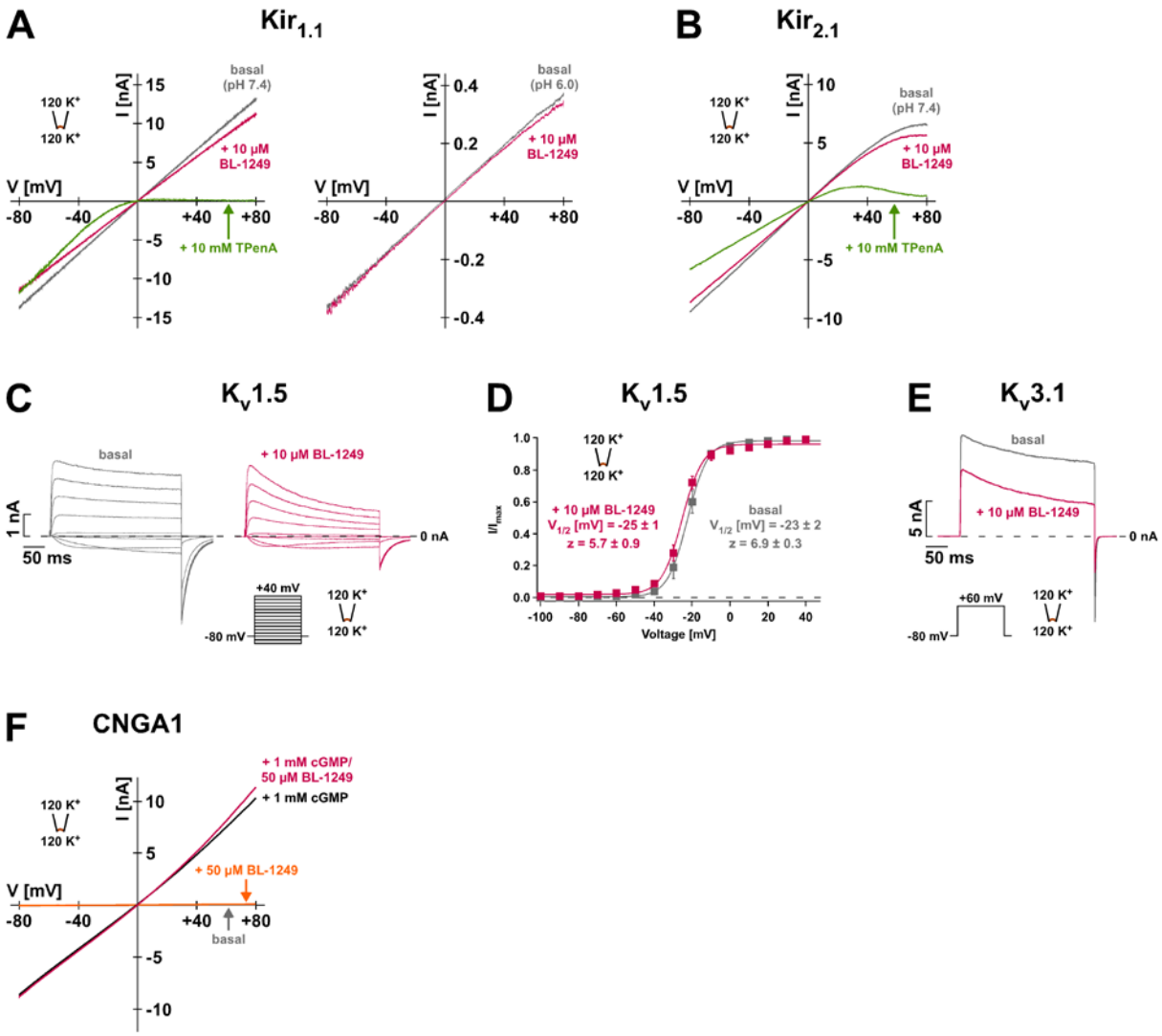

Fig. S2. BL-1249 fails to activate K^+ channels gated at the lower helix-bundle crossing and SF-gated CNG channels.

Fig. S2. BL-1249 fails to activate K^+ channels gated at the lower helix-bundle crossing and SF-gated CNG channels. The effect of BL-1249 on K^+ channels that use the helix-bundle crossing as an activation gate (i.e. K_{ir} and K_v channels) was tested in i-o patches from channels expressed in *Xenopus* oocytes. (**A**) Representative $K_{ir}1.1$ currents evoked by voltage ramps from -80 mV to +80 mV at pH 7.4 (strong pH_i activation) and pH 6.0 (weak pH_i activation) of the same patch without (basal) and with 10 µM BL-1249 as indicated. Voltage-dependent inhibition by 10 mM TPenA is shown to demonstrate typical $K_{ir}1.1$ activity. (**B**) $K_{ir}2.1$ currents evoked by identical voltage ramps at pH 7.4 without (basal) and with 10 µM BL-1249. Voltage-dependent inhibition by 10 mM TPenA is shown to demonstrate a typical $K_{ir}2.1$ response. (**C**) $K_v1.5$ currents evoked by voltage steps from -100 mV to +40 mV with 10 mV increments as depicted without (basal) and with 10 µM BL-1249. Note BL-1249 causes a weak transient inhibition (similar to open channel block), but no activation is

apparent by comparing the tail current/voltage relationship (**D**) ± 10 µM BL-1249 (i.e. no shift in $V_{1/2}$ of voltage activation; n ≥ 11). (**E**) K_v3.1 currents evoked by depolarization from a holding potential of -80 mV to +60 mV and back as indicated ± 10 µM BL-1249. Note BL-1249 causes a weak transient inhibition and ~30 % block of the initial outward current. (**F**) The effect of 50 µM BL-1249 on representative basal currents ± 1 mM cGMP for CNGA1 channels measured in i-o patches.

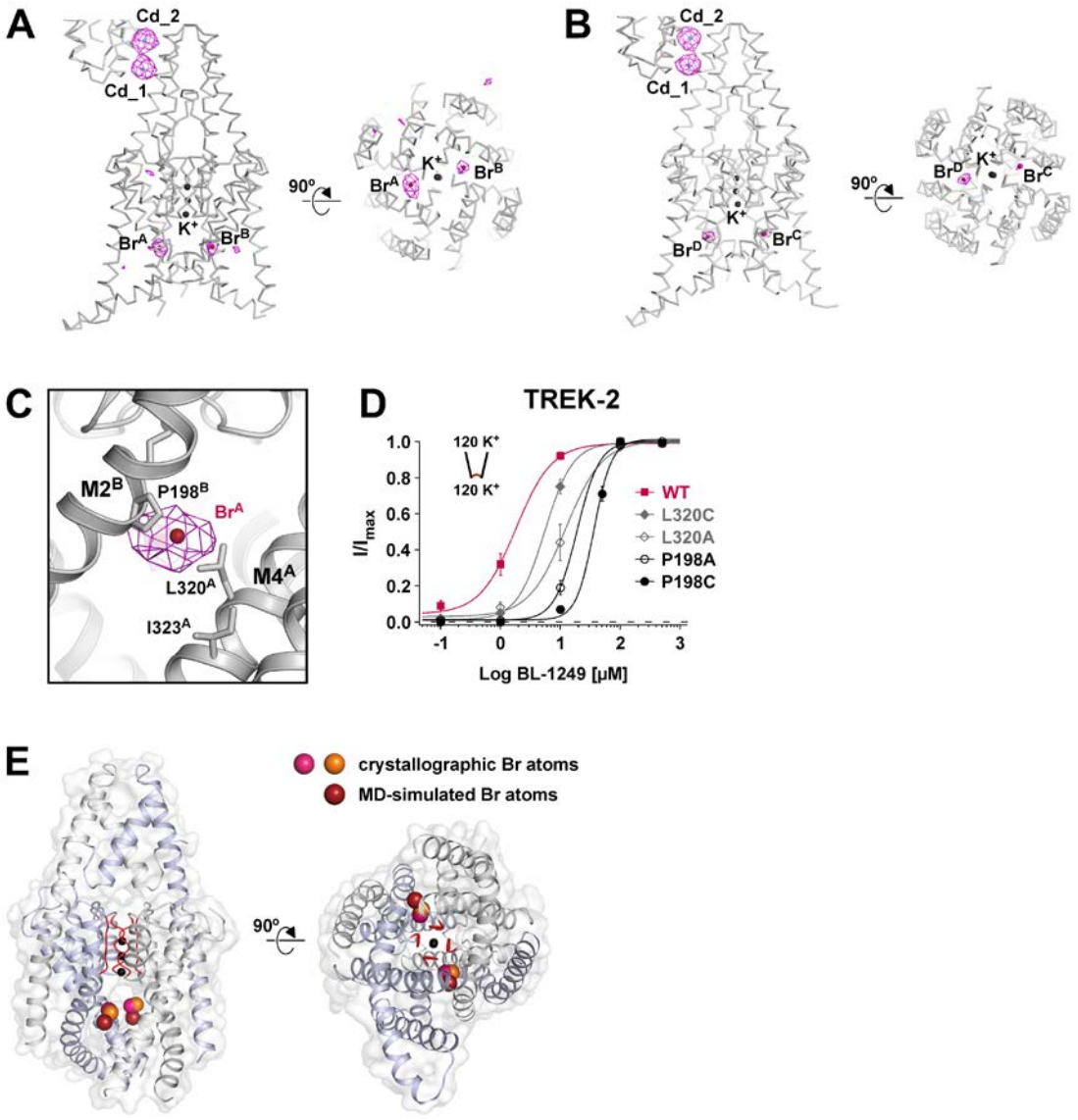

Fig. S3. Positions of BL-1249 Br atoms in TREK-2 K_{2P} dimers based on anomalous difference peaks.

Fig. S3. Positions of BL-1249 Br atoms in TREK-2 K_{2P} dimers based on anomalous difference peaks. (**A** and **B**) Crystallographically determined positions of bromine atoms of BL-1249^{Br} are shown for the two dimers present in the asymmetric unit (AB/CD). A 6 Å anomalous difference Fourier map calculated using phases from the PHASER molecular

replacement solution is contoured at 3.3 σ (magenta mesh) and overlaid on the Cα trace of the partially refined PHASER solution. The highest anomalous peaks correspond to two cadmium ions (Cd_1/Cd_2) from the crystallization solution bound between the cap domains of each dimer. The next highest peaks in the map represent the bromine positions (Br^A/Br^B/Br^C/Br^D). Two perpendicular views are shown for each dimer looking from the plane of the membrane (left) and from the cytoplasmic face (right). (**C**) Zoomed-in view of the Br position in the AB dimer located between helix $M2^B$ and $M4^A$. (**D**) BL-1249 dose-response curves for TREK-2 WT (n = 13) and mutations (P198C or P198A (n = 14), L320C or L320A (n = 6)) reducing BL-1249 activation and positioned close to the bromine. These residues are homologous to the TREK-1 mutations shown in Fig. 2D. (**E**) Comparison of the four crystallographically determined BL-1249 Br atoms (Br^A/Br^B (pink) Br^C/Br^D (orange)) after superposition of the two dimers and those derived from the MD simulation (brown).

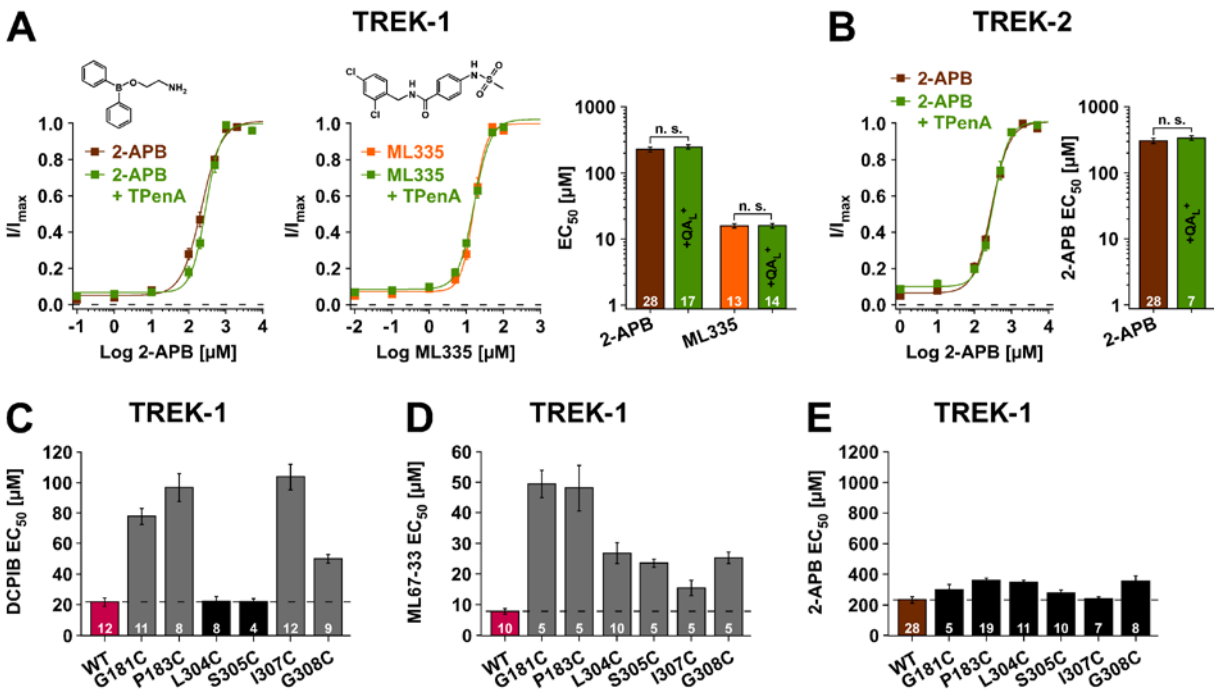

Fig. S4. Specifity of the NCA QA_L^+ competition assay and the BL-1249 binding site mutations.

Fig. S4. Specificity of the NCA QA_L^+ competition assay and the BL-1249 binding site mutations. (**A**) Dose-response curves for activation of TREK-1 by 2-APB (left; brown curve) and ML335 (middle; orange curve) ± 80 µM TPenA (green curve) producing ~71 to 77 % inhibition of the basal current at +40 mV; right: bars represent EC_{50} values ± S.E.M for 2-APB and ML335 activation ± TPenA obtained from data as shown in the left and middle panels. Note ML335 and 2-APB have been shown to bind at sites outside of the inner cavity.

(**B**) Dose-response curves of TREK-2 channel activation by 2-APB ± 80 µM TPenA producing 76 ± 2 % inhibition of the basal current; right: bars represent EC_{50} values ± S.E.M for 2-APB activation ± TPenA obtained from the data as shown in the left panel. (**C**), (**D**), (**E**) Bars represent EC_{50} values ± S.E.M for activation by DCPIB (**C**), by ML67-33 (**D**) and by 2-APB (**E**) of TREK-1 WT channels and indicated mutants that reduce BL-1249 activation (see also Fig. 2D).

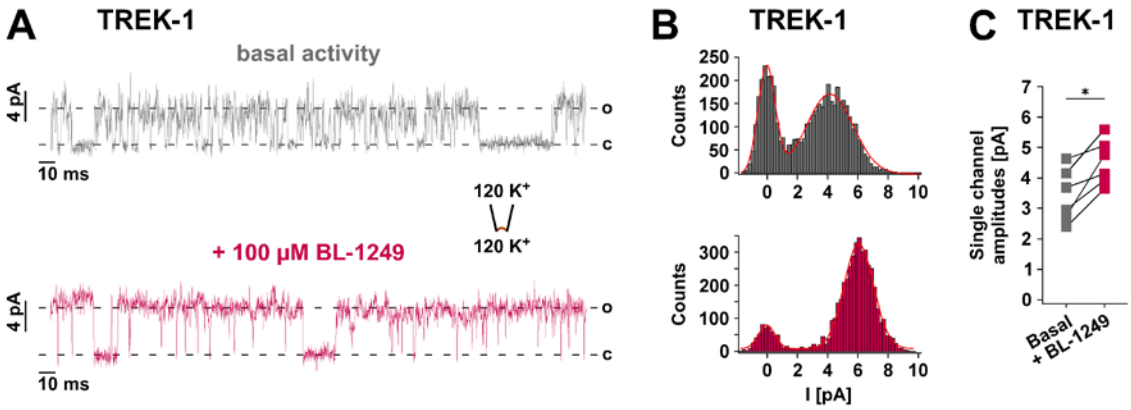

Fig. S5. BL-1249 effect on TREK-1 single channel currents.

Fig. S5. BL-1249 effect on TREK-1 single channel currents. (**A**) Representative TREK-1 single channel current traces measured in the same i-o patches from *Xenopus* oocytes at +60 mV before application (upper trace; basal activity) and after application of 100 µM BL-1249 (lower trace). (**B**) Example current amplitude histograms corresponding to the recordings shown in (A) and fitted with a Gaussian function to obtain the single channel amplitudes that are plotted for individual recordings before and after BL-1249 in (**C**).

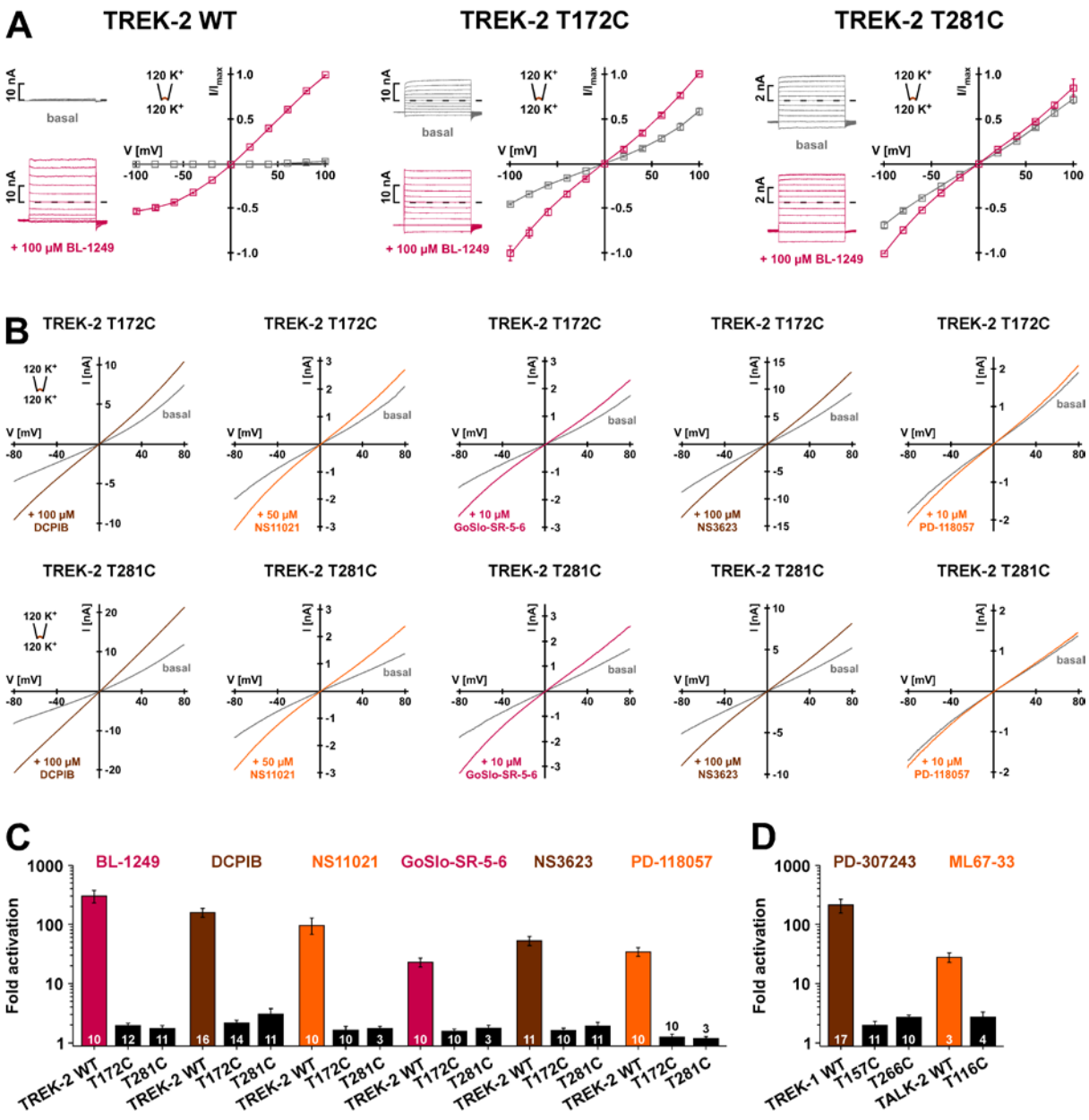

Fig. S6. Mutations at the SF render K_{2P} channels insensitive to drug activation.

Fig. S6. Mutations at the SF render K_{2P} channels insensitive to drug activation. (**A**) Currents in i-o patches in response to voltage steps (from -100 mV to +100 mV) for WT TREK-2 channels and indicated mutants without (basal) and with 100 µM BL-1249; from these mean data IVs ± S.E.M are plotted. (**B**) Representative IVs for TREK-2 T172C and T281C currents ± the indicated activator. (**C**) and (**D**) Bars represent fold activation ± S.E.M at -80 mV upon application of indicated compounds (10 µM PD-118057 and GoSlo-SR-5-6, 50 µM NS11021 and 100 µM BL-1249, DCPIB, NS3623, PD-307243 and ML67-33) for indicated K_{2P} channels and respective mutants (mutations substitute the conserved SF threonines that coordinate the S4 K^+ ion in the SF as previously reported (*17*)).

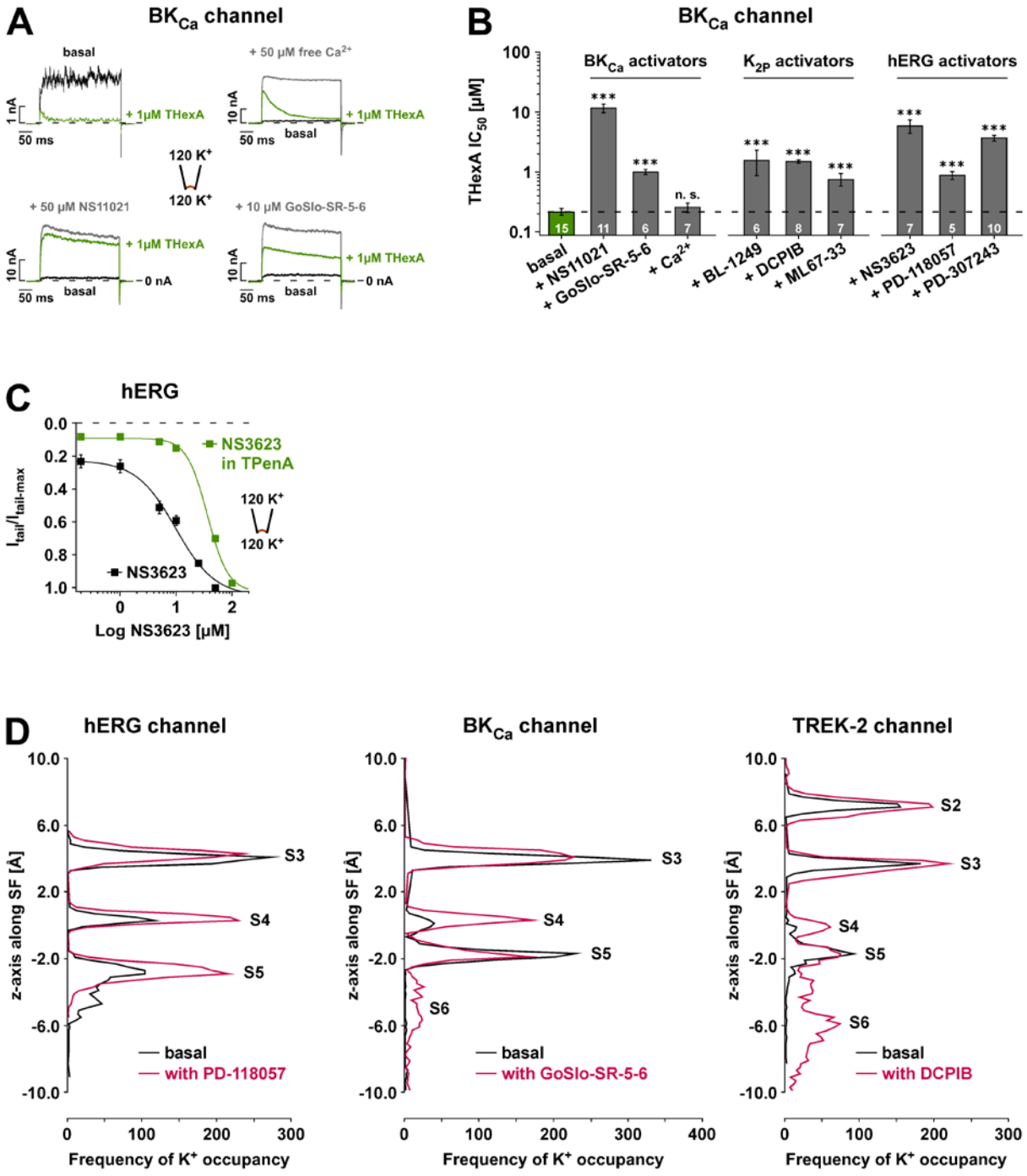

Fig. S7. NCAs compete with QA_L^+ in BK_{Ca} and hERG channels and change the SF K^+ occupancy in hERG, BK_{Ca} and TREK-2.

Fig. S7. NCAs compete with QA_L^+ in BK_{Ca} and hERG channels and change the SF K^+ occupancy in hERG, BK_{Ca} and TREK-2. (**A**) BK_{Ca} currents in i-o patches evoked by voltage steps (from -80 mV to +100 mV) with THexA applied to basal currents (upper left traces), applied to Ca^{2+} activated BK_{Ca} currents (upper right traces); NS11021 activated BK_{Ca} currents (lower left traces) and GoSlo-SR-5-6 activated currents (lower right traces). (**B**) Bars

represent the IC_{50} value ± S.E.M. for THexA inhibition obtained from THexA dose-response curves for basal currents (indicated as dotted line) and subsequent to activation by 50 µM NS11021, 10 µM GoSlo-SR-5-6, 50 µM free Ca^{2+}, 100 µM BL-1249, 100 µM DCPIB, 50 µM ML67-33, 50 µM NS3623, 10 µM PD-118057, 50 µM PD-307243. (**C**) NS3623 dose-response curves represent normalized tail currents ± 1 µM TPenA that produced 84 ± 3 % inhibition of basal currents ($n \geq 8$). (**D**) The relative K^+ occupancies for the indicated K^+ sites (S2 to S6) obtained from MD simulations of hERG, BK_{Ca} and TREK-2 channels with the respective compounds docked in their favoured poses (orange) and their occupancies in the apo-structures (black lines). Note that (i) MD simulations are performed without applied voltage gradient (in contrast to Fig. 3, A and B), (ii) the K^+ occupancies differ for the three apo-structures, and (iii) for BK_{Ca} and TREK-2 channels NCA binding increases the S6 occupancy (with the other changes in SF occupancy are likely promoted by the S6 increase) while in hERG channels the S5 occupancy is increased consistent with the position of the negative charge of the NCA being localized further upward towards the SF and, thus, closer to the S5 K^+ ion.

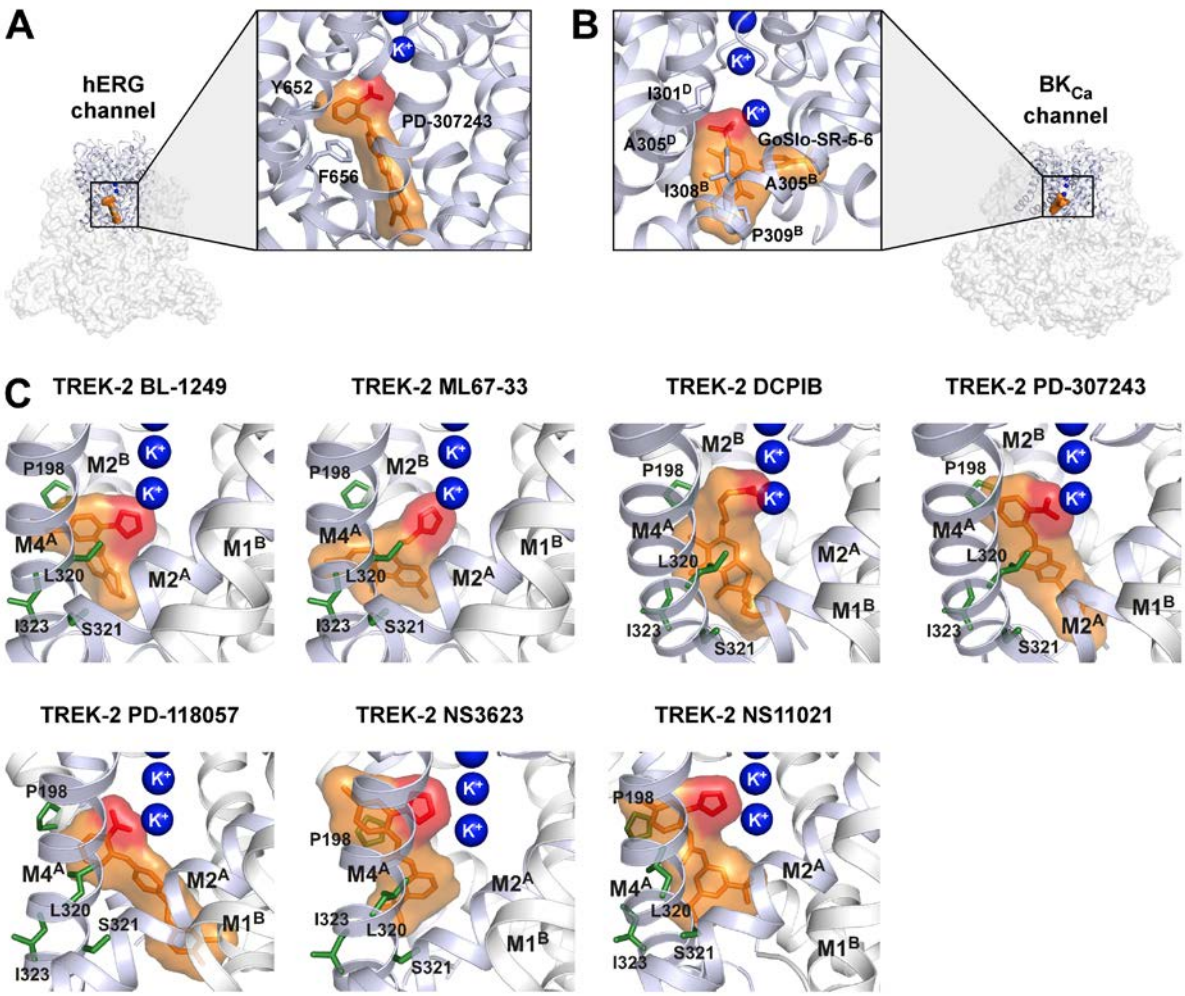

Fig. S8. NCA binding poses in hERG, BK_{Ca} and TREK-2 K_{2P} channels.

Fig. S8. NCA binding poses in hERG, BK_{Ca} and TREK-2 K_{2P} channels. (**A**) Structure of the hERG channel (PDB ID: 5VA1) depicted as shadow surface with the pore region highlighted (light blue) used for MD simulations to obtain the favoured binding pose of PD-307243 (orange) with the carboxylate group (red) interacting with a K^+ ion as illustrated. (**B**) Structure of the BK_{Ca} channel (PDB ID: 5TJI) with the pore region highlighted used for MD simulations to obtain the favoured binding pose of GoSlo-SR-5-6 (orange) as depicted in the magnification with the sulphonate group (red) interacting with a K^+ ion in the cavity. (**C**) Structural representation of the favoured binding poses of the indicated compounds obtained from MD simulation performed on TREK-2; the corresponding TREK-1 residues that markedly reduce BL-1249 activation are highlighted (green). The negatively charged groups of the compounds are coloured (red) to indicate their proximity to the depicted K^+ ions.

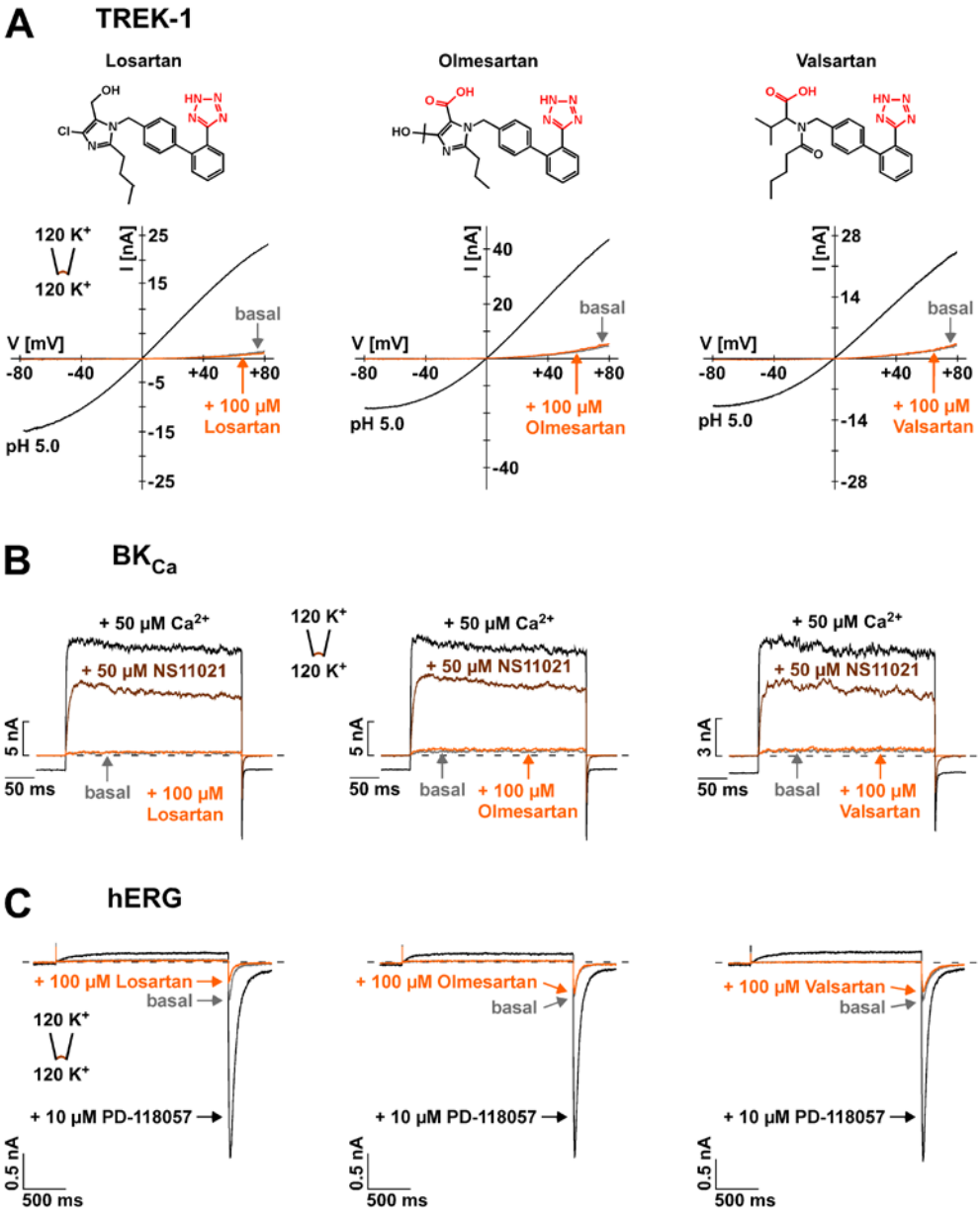

Fig. S9. Negatively charged compounds that do not fit the NCA pharmacophore fail to activate TREK-1 K_{2P}, BK_{Ca} and hERG channels.

Fig. S9. Tetrazole containing compounds that do not fit the NCA pharmacophore fail to activate TREK-1 K_{2P}, BK_{Ca} and hERG channels. (**A**) Upper panel: the tetrazole and carboxylate group containing compounds losartan, olmesartan and valsartan are depicted. Although very similar in composition, they do not fit the NCA pharmacophore as shown in Fig. 4E; lower panel: TREK-1 currents of i-o patches of *Xenopus* oocytes evoked by voltage ramps from -80 mV to +80 mV without (basal) are not activated by 100 µM of the respective compounds. As a control, TREK-1 currents in the same patches were strongly activated by low pH_i 5.0. (**B**) BK_{Ca} currents in i-o patches evoked by voltage steps (from -80 mV to +100 mV) without (gray trace) and with 100 µM of the respective compounds. As a control, BK_{Ca}

currents in the same patches were activated by 50 µM free Ca^{2+} and 50 µM of the drug NS11021. (**C**) hERG currents in i-o patches evoked by voltage steps (from -80 mV to +60 mV mand back to -100 mV) without (gray trace) and with 100 µM of the respective compounds. As a control, hERG currents in the same patches were activated by 10 µM of the drug PD-118057.

Table S1: Data collection and statistics.

Data collection	**BL-1249^{Br}**
Space group	$P2_1$
Cell dimensions	
a, *b*, *c* (Å)	89.77, 107.62, 106.69
α, β, γ (°)	90, 90.18, 90
Resolution [Å][1]	75 - 3.8 (3.80 - 3.90)[1]
Resolution limits [Å][2]	4.9, 4.1, 3.8 (4.6, 4.1, 3.8)
Nominal resolution [Å][3]	4.1
$CC_{1/2}$	1.000 (0.55)
CC_{anom}	0.57
R_{meas}	0.057 (3.28)[1]
R_{pim}	0.016 (0.88)
$I / \sigma I$	19.7 (0.9)[1]
Completeness [%]	100 (100)[1]
Redundancy	13.3 (13.7)[1]

[1]Values in parentheses are statistics for highest resolution shell

[2]Anisotropic resolution limits along each of the three principal directions as defined by AIMLESS based on Mn (I/sd(I)) > 2. Values in parentheses are resolution limits in each direction based on half dataset correlation > 0.5 ($CC_{1/2}$).

[3]Nominal resolution is defined based on overall Mn (I/sd (I)) > 2.0 $CC_{1/2}$ > 0.50 as estimated by AIMLESS.

Table S2: TREK-1 K_{2P} channel competition assay statistics.

Compound	EC_{50} (µM)	n	QA^+ ion	$EC_{50\ (QAL+)}$ (µM)	n	*P* value
BL-1249	2.64 ± 0.45	24	THexA (5 µM)	66.50 ± 1.82	8	5.78×10^{-6}
ML67-33	8.15 ± 0.75	10	TPenA (80 µM)	64.53 ± 2.54	9	3.92×10^{-5}
DCPIB	22.02 ± 2.71	12	TPenA (80 µM)	121.49 ± 4.35	19	1.49×10^{-7}
PD-118057	3.36 ± 0.76	9	TPenA (80 µM)	14.64 ± 1.19	5	7.31×10^{-5}
PD-307243	14.70 ± 0.99	9	TPenA (80 µM)	83.73 ± 4.30	12	1.62×10^{-5}
NS3623	39.21 ± 10.91	11	TPenA (80 µM)	176.60 ± 16.28	5	1.28×10^{-4}
NS11021	8.05 ± 1.29	7	TPenA (80 µM)	36.84 ± 0.85	5	6.88×10^{-9}
GoSlo-SR-5-6	5.88 ± 0.25	9	TPenA (80 µM)	82.85 ± 17.05	8	1.13×10^{-4}
2-APB	235.27 ± 20.85	28	TPenA (80 µM)	256.74 ± 19.02	21	n. s.
ML335	16.07 ± 0.88	13	TPenA (80 µM)	15.48 ± 0.79	14	n. s.

Table S3: BK_{Ca} channel competition assay statistics.

Compound	IC_{50} (µM)	n	*P* value
THexA	0.22 ± 0.03	15	-
+ NS11021 (50 µM)	11.84 ± 1.99	11	1.28×10^{-6}
+ GoSlo-SR-5-6 (10 µM)	1.00 ± 0.09	6	1.84×10^{-4}
+ BL-1249 (100 µM)	1.56 ± 0.73	6	3.20×10^{-4}
+ DCPIB (100 µM)	1.50 ± 0.08	8	1.23×10^{-5}
+ ML67-33 (50 µM)	0.75 ± 0.18	7	5.27×10^{-4}
+ NS3623 (50 µM)	5.93 ± 1.52	7	3.00×10^{-5}
+ PD-118057 (10 µM)	0.89 ± 0.14	5	2.37×10^{-4}
+ PD-307243 (50 µM)	3.75 ± 0.27	10	2.56×10^{-6}
+ free Ca^{2+} (50 µM)	0.26 ± 0.05	7	n. s.

References and Notes

1. S. I. V. Judge, P. J. Smith, P. E. Stewart, C. T. Bever Jr., Potassium channel blockers and openers as CNS neurologic therapeutic agents. *Recent Pat. CNS Drug Discov.* **2**, 200–228 (2007). doi:10.2174/157488907782411765 Medline

2. V. K. Vyas, P. Parikh, J. Ramani, M. Ghate, Medicinal chemistry of potassium channel modulators: An update of recent progress (2011–2017). *Curr. Med. Chem.* 10.2174/0929867325666180430152023 (2018).

3. S. Hou, S. H. Heinemann, T. Hoshi, Modulation of BK_{Ca} channel gating by endogenous signaling molecules. *Physiology* **24**, 26–35 (2009). doi:10.1152/physiol.00032.2008 Medline

4. M. I. Niemeyer, L. P. Cid, W. González, F. V. Sepúlveda, Gating, regulation, and structure in K_{2P} K^+ channels: *In varietate concordia*? *Mol. Pharmacol.* **90**, 309–317 (2016). doi:10.1124/mol.116.103895 Medline

5. F. V. Sepúlveda, L. Pablo Cid, J. Teulon, M. I. Niemeyer, Molecular aspects of structure, gating, and physiology of pH-sensitive background K_{2P} and Kir K^+-transport channels. *Physiol. Rev.* **95**, 179–217 (2015). doi:10.1152/physrev.00016.2014 Medline

6. G. Yellen, The voltage-gated potassium channels and their relatives. *Nature* **419**, 35–42 (2002). doi:10.1038/nature00978 Medline

7. P. L. Piechotta, M. Rapedius, P. J. Stansfeld, M. K. Bollepalli, G. Ehrlich, I. Andres-Enguix, H. Fritzenschaft, N. Decher, M. S. P. Sansom, S. J. Tucker, T. Baukrowitz, The pore structure and gating mechanism of K2P channels. *EMBO J.* **30**, 3607–3619 (2011). doi:10.1038/emboj.2011.268 Medline

8. S. N. Bagriantsev, R. Peyronnet, K. A. Clark, E. Honoré, D. L. Minor Jr., Multiple modalities converge on a common gate to control K_{2P} channel function. *EMBO J.* **30**, 3594–3606 (2011). doi:10.1038/emboj.2011.230 Medline

9. C. M. Wilkens, R. W. Aldrich, State-independent block of BK channels by an intracellular quaternary ammonium. *J. Gen. Physiol.* **128**, 347–364 (2006). doi:10.1085/jgp.200609579 Medline

10. Y. Zhou, X.-M. Xia, C. J. Lingle, Cysteine scanning and modification reveal major differences between BK channels and Kv channels in the inner pore region. *Proc. Natl. Acad. Sci. U.S.A.* **108**, 12161–12166 (2011). doi:10.1073/pnas.1104150108 Medline

11. P. L. Smith, T. Baukrowitz, G. Yellen, The inward rectification mechanism of the HERG cardiac potassium channel. *Nature* **379**, 833–836 (1996). doi:10.1038/379833a0 Medline

12. J. I. Vandenberg, E. Perozo, T. W. Allen, Towards a structural view of drug binding to hERG K^+ channels. *Trends Pharmacol. Sci.* **38**, 899–907 (2017). doi:10.1016/j.tips.2017.06.004 Medline

13. L. Pope, C. Arrigoni, H. Lou, C. Bryant, A. Gallardo-Godoy, A. R. Renslo, D. L. Minor Jr., Protein and chemical determinants of BL-1249 action and selectivity for K_{2P} channels. *ACS Chem. Neurosci.* **9**, 3153–3165 (2018). doi:10.1021/acschemneuro.8b00337 Medline

14. J. Zhou, C. E. Augelli-Szafran, J. A. Bradley, X. Chen, B. J. Koci, W. A. Volberg, Z. Sun, J. S. Cordes, Novel potent human *ether-à-go-go*-related gene (*hERG*) potassium

channel enhancers and their in vitro antiarrhythmic activity. *Mol. Pharmacol.* **68**, 876–884 (2005). doi:10.1124/mol.105.014035 Medline

15. B. H. Bentzen, A. Nardi, K. Calloe, L. S. Madsen, S.-P. Olesen, M. Grunnet, The small molecule NS11021 is a potent and specific activator of Ca^{2+}-activated big-conductance K^+ channels. *Mol. Pharmacol.* **72**, 1033–1044 (2007). doi:10.1124/mol.107.038331 Medline

16. M. J. Lenaeus, D. Burdette, T. Wagner, P. J. Focia, A. Gross, Structures of KcsA in complex with symmetrical quaternary ammonium compounds reveal a hydrophobic binding site. *Biochemistry* **53**, 5365–5373 (2014). doi:10.1021/bi500525s Medline

17. M. Schewe, E. Nematian-Ardestani, H. Sun, M. Musinszki, S. Cordeiro, G. Bucci, B. L. de Groot, S. J. Tucker, M. Rapedius, T. Baukrowitz, A non-canonical voltage-sensing mechanism controls gating in K2P K^+ channels. *Cell* **164**, 937–949 (2016). doi:10.1016/j.cell.2016.02.002 Medline

18. J. G. McCoy, C. M. Nimigean, Structural correlates of selectivity and inactivation in potassium channels. *Biochim. Biophys. Acta* **1818**, 272–285 (2012). doi:10.1016/j.bbamem.2011.09.007 Medline

19. Y. Y. Dong, A. C. W. Pike, A. Mackenzie, C. McClenaghan, P. Aryal, L. Dong, A. Quigley, M. Grieben, S. Goubin, S. Mukhopadhyay, G. F. Ruda, M. V. Clausen, L. Cao, P. E. Brennan, N. A. Burgess-Brown, M. S. P. Sansom, S. J. Tucker, E. P. Carpenter, K2P channel gating mechanisms revealed by structures of TREK-2 and a complex with Prozac. *Science* **347**, 1256–1259 (2015). doi:10.1126/science.1261512 Medline

20. M. Rapedius, M. R. Schmidt, C. Sharma, P. J. Stansfeld, M. S. P. Sansom, T. Baukrowitz, S. J. Tucker, State-independent intracellular access of quaternary ammonium blockers to the pore of TREK-1. *Channels* **6**, 473–478 (2012). doi:10.4161/chan.22153 Medline

21. R.-G. Zhuo, P. Peng, X.-Y. Liu, H.-T. Yan, J.-P. Xu, J.-Q. Zheng, X.-L. Wei, X.-Y. Ma, Intersubunit concerted cooperative and *cis*-type mechanisms modulate allosteric gating in two-pore-domain potassium channel TREK-2. *Front. Cell. Neurosci.* **10**, 127 (2016). doi:10.3389/fncel.2016.00127 Medline

22. M. Lolicato, C. Arrigoni, T. Mori, Y. Sekioka, C. Bryant, K. A. Clark, D. L. Minor Jr., K_{2P}2.1 (TREK-1)-activator complexes reveal a cryptic selectivity filter binding site. *Nature* **547**, 364–368 (2017). doi:10.1038/nature22988 Medline

23. W. Kopec, D. A. Köpfer, O. N. Vickery, A. S. Bondarenko, T. L. C. Jansen, B. L. de Groot, U. Zachariae, Direct knock-on of desolvated ions governs strict ion selectivity in K^+ channels. *Nat. Chem.* **10**, 813–820 (2018). doi:10.1038/s41557-018-0105-9 Medline

24. M. V. Clausen, V. Jarerattanachat, E. P. Carpenter, M. S. P. Sansom, S. J. Tucker, Asymmetric mechanosensitivity in a eukaryotic ion channel. *Proc. Natl. Acad. Sci. U.S.A.* **114**, E8343–E8351 (2017). doi:10.1073/pnas.1708990114 Medline

25. D. Kang, C. Choe, D. Kim, Thermosensitivity of the two-pore domain K^+ channels TREK-2 and TRAAK. *J. Physiol.* **564**, 103–116 (2005). doi:10.1113/jphysiol.2004.081059 Medline

26. M. Zhou, R. MacKinnon, A mutant KcsA K^+ channel with altered conduction properties and selectivity filter ion distribution. *J. Mol. Biol.* **338**, 839–846 (2004). doi:10.1016/j.jmb.2004.03.020 Medline

27. S. N. Bagriantsev, K.-H. Ang, A. Gallardo-Godoy, K. A. Clark, M. R. Arkin, A. R. Renslo, D. L. Minor Jr., A high-throughput functional screen identifies small molecule regulators of temperature- and mechano-sensitive K_{2P} channels. *ACS Chem. Biol.* **8**, 1841–1851 (2013). doi:10.1021/cb400289x Medline

28. L. Minieri, H. Pivonkova, M. Caprini, L. Harantova, M. Anderova, S. Ferroni, The inhibitor of volume-regulated anion channels DCPIB activates TREK potassium channels in cultured astrocytes. *Br. J. Pharmacol.* **168**, 1240–1254 (2013). doi:10.1111/bph.12011 Medline

29. E. Gordon, I. M. Lozinskaya, Z. Lin, S. F. Semus, F. E. Blaney, R. N. Willette, X. Xu, 2-[2-(3,4-dichloro-phenyl)-2,3-dihydro-1*H*-isoindol-5-ylamino]-nicotinic acid (PD-307243) causes instantaneous current through human *ether-a-go-go*-related gene potassium channels. *Mol. Pharmacol.* **73**, 639–651 (2008). doi:10.1124/mol.107.041152 Medline

30. R. S. Hansen, T. G. Diness, T. Christ, E. Wettwer, U. Ravens, S.-P. Olesen, M. Grunnet, Biophysical characterization of the new human ether-a-go-go-related gene channel opener NS3623 [*N*-(4-bromo-2-(1*H*-tetrazol-5-yl)-phenyl)-*N*′-(3′-trifluoromethylphenyl)urea]. *Mol. Pharmacol.* **70**, 1319–1329 (2006). doi:10.1124/mol.106.026492 Medline

31. S. Roy, A. Morayo Akande, R. J. Large, T. I. Webb, C. Camarasu, G. P. Sergeant, N. G. McHale, K. D. Thornbury, M. A. Hollywood, Structure-activity relationships of a novel group of large-conductance Ca^{2+}-activated K^+ (BK) channel modulators: The GoSlo-SR family. *ChemMedChem* **7**, 1763–1769 (2012). doi:10.1002/cmdc.201200321 Medline

32. W. Wang, R. MacKinnon, Cryo-EM structure of the open human *ether-à-go-go*-related K^+ channel hERG. *Cell* **169**, 422–430.e10 (2017). doi:10.1016/j.cell.2017.03.048 Medline

33. V. Pau, Y. Zhou, Y. Ramu, Y. Xu, Z. Lu, Crystal structure of an inactivated mutant mammalian voltage-gated K^+ channel. *Nat. Struct. Mol. Biol.* **24**, 857–865 (2017). doi:10.1038/nsmb.3457 Medline

34. H. Yang, G. Zhang, J. Cui, BK channels: Multiple sensors, one activation gate. *Front. Physiol.* **6**, 29 (2015). doi:10.3389/fphys.2015.00029 Medline

35. D. Simkin, E. J. Cavanaugh, D. Kim, Control of the single channel conductance of K_{2P}10.1 (TREK-2) by the amino-terminus: Role of alternative translation initiation. *J. Physiol.* **586**, 5651–5663 (2008). doi:10.1113/jphysiol.2008.161927 Medline

36. W. Kabsch, XDS. *Acta Crystallogr. D Biol. Crystallogr.* **66**, 125–132 (2010). doi:10.1107/S0907444909047337 Medline

37. P. Evans, Scaling and assessment of data quality. *Acta Crystallogr. D Biol. Crystallogr.* **62**, 72–82 (2006). doi:10.1107/S0907444905036693 Medline

38. A. J. McCoy, R. W. Grosse-Kunstleve, P. D. Adams, M. D. Winn, L. C. Storoni, R. J. Read, Phaser crystallographic software. *J. Appl. Crystallogr.* **40**, 658–674 (2007). doi:10.1107/S0021889807021206 Medline

39. G. Bricogne, E. Blanc, M. T. Brandl, C. Flensburg, P. Keller, W. Paciorek, P. Roversi, A. Sharff, O. S. Smart, C. Vonrhein, BUSTER version 2.10.0. (Global Phasing Limited, 2017).

40. S. G. Brohawn, E. B. Campbell, R. MacKinnon, Domain-swapped chain connectivity and gated membrane access in a Fab-mediated crystal of the human TRAAK K^+ channel.

Proc. Natl. Acad. Sci. U.S.A. **110**, 2129–2134 (2013). doi:10.1073/pnas.1218950110 Medline

41. R. K. Hite, X. Tao, R. MacKinnon, Structural basis for gating the high-conductance Ca^{2+}-activated K^+ channel. *Nature* **541**, 52–57 (2017). doi:10.1038/nature20775 Medline

42. A. Šali, T. L. Blundell, Comparative protein modelling by satisfaction of spatial restraints. *J. Mol. Biol.* **234**, 779–815 (1993). doi:10.1006/jmbi.1993.1626 Medline

43. J. Chen, G. Seebohm, M. C. Sanguinetti, Position of aromatic residues in the S6 domain, not inactivation, dictates cisapride sensitivity of HERG and eag potassium channels. *Proc. Natl. Acad. Sci. U.S.A.* **99**, 12461–12466 (2002). doi:10.1073/pnas.192367299 Medline

44. J. S. Mitcheson, J. Chen, M. Lin, C. Culberson, M. C. Sanguinetti, A structural basis for drug-induced long QT syndrome. *Proc. Natl. Acad. Sci. U.S.A.* **97**, 12329–12333 (2000). doi:10.1073/pnas.210244497 Medline

45. M. Perry, M. J. de Groot, R. Helliwell, D. Leishman, M. Tristani-Firouzi, M. C. Sanguinetti, J. Mitcheson, Structural determinants of HERG channel block by clofilium and ibutilide. *Mol. Pharmacol.* **66**, 240–249 (2004). doi:10.1124/mol.104.000117 Medline

46. Small-Molecule Drug Discovery Suite (Schrödinger, New York, 2017).

47. K. Lindorff-Larsen, S. Piana, K. Palmo, P. Maragakis, J. L. Klepeis, R. O. Dror, D. E. Shaw, Improved side-chain torsion potentials for the Amber ff99SB protein force field. *Proteins* **78**, 1950–1958 (2010). doi:10.1002/prot.22711 Medline

48. P. Mark, L. Nilsson, Structure and dynamics of the TIP3P, SPC, and SPC/E water models at 298 K. *J. Phys. Chem. A* **105**, 9954–9960 (2001). doi:10.1021/jp003020w

49. I. S. Joung, T. E. Cheatham 3rd, Determination of alkali and halide monovalent ion parameters for use in explicitly solvated biomolecular simulations. *J. Phys. Chem. B* **112**, 9020–9041 (2008). doi:10.1021/jp8001614 Medline

50. O. Berger, O. Edholm, F. Jähnig, Molecular dynamics simulations of a fluid bilayer of dipalmitoylphosphatidylcholine at full hydration, constant pressure, and constant temperature. *Biophys. J.* **72**, 2002–2013 (1997). doi:10.1016/S0006-3495(97)78845-3 Medline

51. J. Wang, R. M. Wolf, J. W. Caldwell, P. A. Kollman, D. A. Case, Development and testing of a general amber force field. *J. Comput. Chem.* **25**, 1157–1174 (2004). doi:10.1002/jcc.20035 Medline

52. J. Wang, W. Wang, P. A. Kollman, D. A. Case, Automatic atom type and bond type perception in molecular mechanical calculations. *J. Mol. Graph. Model.* **25**, 247–260 (2006). doi:10.1016/j.jmgm.2005.12.005 Medline

53. C. I. Bayly, P. Cieplak, W. Cornell, P. A. Kollman, A well-behaved electrostatic potential based method using charge restraints for deriving atomic charges: The RESP model. *J. Phys. Chem.* **97**, 10269–10280 (1993). doi:10.1021/j100142a004

54. C. Ballatore, D. M. Huryn, A. B. Smith 3rd, Carboxylic acid (bio)isosteres in drug design. *ChemMedChem* **8**, 385–395 (2013). doi:10.1002/cmdc.201200585 Medline

55. B. Hess, C. Kutzner, D. van der Spoel, E. Lindahl, GROMACS 4: Algorithms for highly efficient, load-balanced, and scalable molecular simulation. *J. Chem. Theory Comput.* **4**, 435–447 (2008). doi:10.1021/ct700301q Medline

56. S. Pronk, S. Páll, R. Schulz, P. Larsson, P. Bjelkmar, R. Apostolov, M. R. Shirts, J. C. Smith, P. M. Kasson, D. van der Spoel, B. Hess, E. Lindahl, GROMACS 4.5: A high-throughput and highly parallel open source molecular simulation toolkit. *Bioinformatics* **29**, 845–854 (2013). doi:10.1093/bioinformatics/btt055 Medline

57. T. Darden, D. York, L. Pedersen, Particle mesh Ewald: An *N*·log(*N*) method for Ewald sums in large systems. *J. Chem. Phys.* **98**, 10089–10092 (1993). doi:10.1063/1.464397

58. U. Essmann, L. Perera, M. L. Berkowitz, T. Darden, H. Lee, L. G. Pedersen, A smooth particle mesh Ewald method. *J. Chem. Phys.* **103**, 8577–8593 (1995). doi:10.1063/1.470117

59. G. Bussi, D. Donadio, M. Parrinello, Canonical sampling through velocity rescaling. *J. Chem. Phys.* **126**, 014101 (2007). doi:10.1063/1.2408420 Medline

60. M. Parrinello, A. Rahman, Polymorphic transitions in single crystals: A new molecular dynamics method. *J. Appl. Phys.* **52**, 7182–7190 (1981). doi:10.1063/1.328693

61. S. Nosé, M. L. Klein, Constant pressure molecular dynamics for molecular systems. *Mol. Phys.* **50**, 1055–1076 (1983). doi:10.1080/00268978300102851

62. B. Hess, H. Bekker, H. J. C. Berendsen, J. G. E. M. Fraaije, LINCS: A linear constraint solver for molecular simulations. *J. Comput. Chem.* **18**, 1463–1472 (1997). doi:10.1002/(SICI)1096-987X(199709)18:12<1463:AID-JCC4>3.0.CO;2-H

63. C. Kutzner, H. Grubmüller, B. L. de Groot, U. Zachariae, Computational electrophysiology: The molecular dynamics of ion channel permeation and selectivity in atomistic detail. *Biophys. J.* **101**, 809–817 (2011). doi:10.1016/j.bpj.2011.06.010 Medline

64. D. P. Tieleman, H. J. C. Berendsen, Molecular dynamics simulations of a fully hydrated dipalmitoylphosphatidylcholine bilayer with different macroscopic boundary conditions and parameters. *J. Chem. Phys.* **105**, 4871–4880 (1996). doi:10.1063/1.472323

65. D. A. Köpfer, C. Song, T. Gruene, G. M. Sheldrick, U. Zachariae, B. L. de Groot, Ion permeation in K^+ channels occurs by direct Coulomb knock-on. *Science* **346**, 352–355 (2014). doi:10.1126/science.1254840 Medline

66. Schrödinger Release 2017-1: Glide (Schrödinger, LLC, New York, 2017).

67. S. Durdagi, I. Erol, R. E. Salmas, M. Patterson, S. Y. Noskov, First universal pharmacophore model for hERG1 K^+ channel activators: acthER. *J. Mol. Graph. Model.* **74**, 153–170 (2017). doi:10.1016/j.jmgm.2017.03.020 Medline